Tectonics

RESEARCH ARTICLE
10.1029/2021TC007078

Key Points:

- Evolution of forearc basins controlled by slab advance and steepening
- Subsidence of back-arc basins controlled by slab roll-back and mantle flow
- Insights into the evolution of Mediterranean forearc and back-arc basin systems

Supporting Information:

Supporting Information may be found in the online version of this article.

Correspondence to:

A. Balázs,
attila.balazs@erdw.ethz.ch

Citation:

Balázs, A., Faccenna, C., Gerya, T., Ueda, K., & Funiciello, F. (2022). The dynamics of forearc – back-arc basin subsidence: Numerical models and observations from Mediterranean subduction zones. *Tectonics*, *41*, e2021TC007078. https://doi.org/10.1029/2021TC007078

Received 16 SEP 2021
Accepted 2 MAY 2022

Author Contributions:

Conceptualization: A. Balázs, C. Faccenna, T. Gerya, F. Funiciello
Funding acquisition: C. Faccenna, T. Gerya, F. Funiciello
Methodology: A. Balázs, T. Gerya, K. Ueda
Project Administration: C. Faccenna, T. Gerya, F. Funiciello
Resources: T. Gerya, F. Funiciello
Software: T. Gerya, K. Ueda
Supervision: C. Faccenna, T. Gerya
Validation: A. Balázs, C. Faccenna, F. Funiciello
Visualization: A. Balázs, K. Ueda
Writing – original draft: A. Balázs
Writing – review & editing: C. Faccenna, T. Gerya, K. Ueda, F. Funiciello

The Dynamics of Forearc – Back-Arc Basin Subsidence: Numerical Models and Observations From Mediterranean Subduction Zones

A. Balázs[1], C. Faccenna[2,3], T. Gerya[1], K. Ueda[1], and F. Funiciello[2]

[1]Department of Earth Sciences, ETH Zürich, Zürich, Switzerland, [2]Department of Sciences, Università Roma Tre, Rome, Italy, [3]GFZ Potsdam, Potsdam, Germany

Abstract The subsidence history of forearc and back-arc basins reflects the relationship between subduction kinematics, mantle dynamics, magmatism, crustal tectonics, and surface processes. The distinct contributions of these processes to the topography variations of active margins during subduction initiation, oceanic subduction, and collision are less understood. We ran 2D elasto-visco-plastic numerical models including surface and hydration processes. The models show the evolution of wedge-top and retro-forearc basins on the continental overriding plate, separated by a forearc high. They are affected by repeated compression and extension phases. Compression-induced subsidence is recorded in the syncline structure of the retro-forearc basin from the onset of subduction. The 2–4 km upper plate negative residual topography is produced by the gradually steepening slab, which drags down the upper plate. Trench retreat leads to slab unbending and decreasing slab dip angle that leads to upper plate trench-ward tilting. Back-arc basins are either formed along inherited weak zones at a large distance from the arc or are created above the hydrated mantle wedge originating from arc rifting. Back-arc subsidence is primarily governed by crustal thinning that is controlled by slab roll-back and supported by the underlying mantle convection. High subduction and mantle convection velocities result in large wavelength negative dynamic topography. Collision and continental subduction are linked to the uplift of the forearc basins; however, the back-arc records ongoing extension during a soft collision. During the hard collision, both the forearc and back-arc basins are ultimately affected by the compression. Our modeling results provide insights into the evolution of Mediterranean subduction zones.

Plain Language Summary In this study, we assess the physical and thermal parameters of the interior of our planet Earth by comparing the topographic variations, that is, subsidence and uplift patterns of high-resolution numerical models and observations from the Mediterranean region of Europe. We particularly focus on subduction zones. These noteworthy regions experience the sinking of dense oceanic tectonic plates beneath less dense upper plates and are characterized by distinct uplift and subsidence patterns. Understanding these processes is important for evaluating seismic risk, but these regions also host important geo-resources, including geothermal energy.

1. Introduction

The topography and thermal history of Earth are controlled by the inherent links between lithospheric and crustal tectonics, mantle convection, and surface processes, such as erosion and sedimentation coupled to climatic variations (Burov, 2011; Whipple, 2009). Topography is mostly governed by isostasy, depending on the thickness and density of the crust and lithosphere (Holmes, 1944). However, along subduction zones the topography of the overriding plate strikingly differs from isostatic predictions, producing kilometer-scale residual, non-isostatic topography (Braun, 2010; Faccenna & Becker, 2020; Flament et al., 2013). Furthermore, several convergent margins have recorded sudden changes in their vertical motions that are still enigmatic, and the origin of related sedimentary basins is less understood (e.g., Mannu et al., 2017; Menant et al., 2020; Noda, 2016).

Sedimentary basins formed on the upper plate of subduction zones are commonly classified into forearc and back-arc basins based on their position with respect to the active volcanic arc (Figure 1; Karig, 1971). Forearc basins overlying the landward side of the accretionary wedge are often called wedge-top forearc basins, while depocenters being formed on the overriding plate are classified as retro-arc or retro-forearc basins (Fuller et al., 2006; Mannu et al., 2017; Noda, 2016). Seismic stratigraphic interpretation of these basins infers repeated phases of extension and contraction superimposed on the overall convergent margin evolution, accretionary

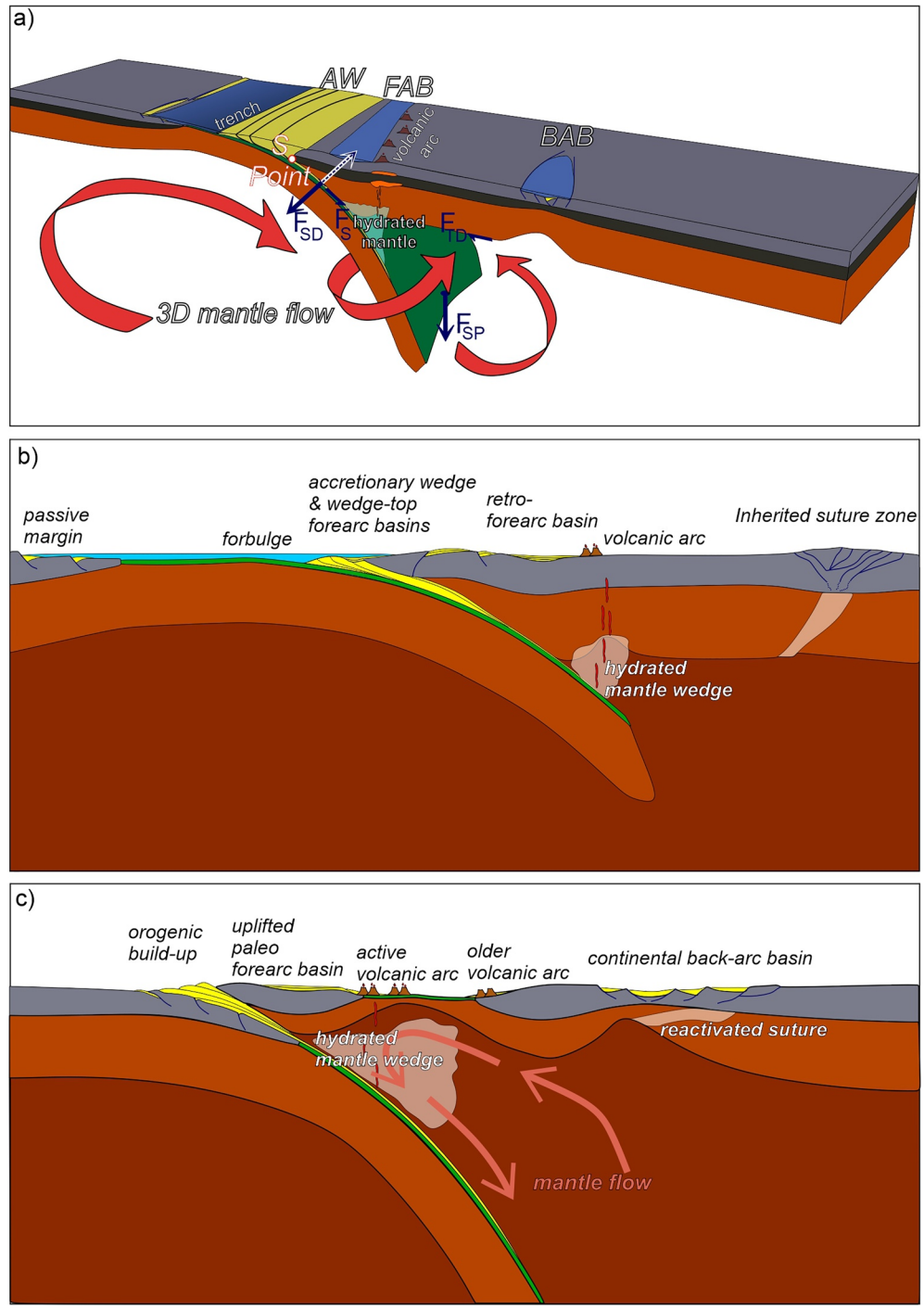

Figure 1. (a) Simplified sketch of a subduction zone, forearc (FAB), and back-arc (BAB) basins and their main driving forces. Sediments are partly accumulated in the trench building up the accretionary wedge (AW) and are partly subducted deeper. F_{SD} – slab induced dragging acting along the subduction interface at the base of the upper plate during slab steepening or pushing during decreasing slab dip angle, respectively. F_{SP} – slab pull force acting on the slab (Forsyth & Uyeda, 1975). F_{TD} – Force generated by the trench-ward mantle drag acting on the base of the upper plate. F_S – Shear force acting on the base of the upper plate driven by the subducting plate. Subduction is inherently linked to mantle flow around the slab. S-point – singularity point marking the upper edge of the upper and lower plate contact. (b) Early stage of oceanic subduction is associated with the development of wedge-top forearc basins and negative residual topography in the retro-forearc basin, volcanism above the hydrated mantle wedge, and incipient strain localization along inherited structures. (c) During mature stage of oceanic and early phase of continental subduction, the forearc basins are uplifted and back-arc basins are formed by reactivation of the inherited weak structures or between the older volcanic and the new volcanic arc following arc rifting.

wedge growth, and sea-level variations (e.g., Mannu et al., 2017; Moore et al., 2015). Furthermore, the observed 1.5–5 km negative residual topography that cannot be solely accommodated by crustal-scale faults are often linked to downward mantle flow or downward suction of the oceanic slab (e.g., Chen et al., 2015; Dickinson & Seely, 1979; Husson, 2006).

Extensional back-arc basins develop in the hinterland of orogenic or volcanic arcs and are driven by crustal and lithospheric thinning when the subduction velocity outpaces the convergence velocity (Dewey et al., 1989). Extensional stress is supposedly linked to trench retreat and slab roll-back coupled to mantle flow toward the retreating slab (e.g., Forsyth & Uyeda, 1975; Wallace et al., 2009). Extensional deformation and crustal thinning are localized along weak zones either along the volcanic arc leading to arc rifting and spreading (e.g., Dymkova et al., 2016; Karig, 1971) or flanking collision zones (Li et al., 2013; Wallace et al., 2009). Furthermore, continental back-arc extension is often localized at larger distances along inherited crustal or lithospheric structures (e.g., Dal Zilio et al., 2018; Shemenda, 1993; Ustaszewski et al., 2010; Yang et al., 2021). Subsidence and uplift patterns of the forearc and back-arc regions are influenced by a wide range of parameters that are linked to the stress transfer from the subducting plate toward the upper plate through the subduction interface or the mantle wedge (Billen & Gurnis, 2001; Davies, 1981).

Geodynamic models help to understand the potential contribution of different parameters to the topography and deformation along subduction zones, such as the role of different slab dip angles (e.g., Chen et al., 2017; Crameri et al., 2017; Zhong & Gurnis, 1992), mantle viscosities (Billen & Gurnis, 2001), subduction interface strength (Buiter et al., 2001; Shemenda, 1993; Zhong & Gurnis, 1994), rheology and deformation of the upper and lower plates (Capitanio et al., 2010; Conrad & Hager, 1999; van Dinther et al., 2019; Fuller et al., 2006; Pusok & Kaus, 2015; Wolf & Huismans, 2019), mantle flow (Espurt et al., 2008; Funiciello et al., 2003; Husson, 2006; Husson et al., 2012; Schellart et al., 2007), elasticity (Hassani et al., 1997), hydration and melting (Faccenda et al., 2009; Sizova et al., 2010; Vogt et al., 2012), and their links to erosion and sedimentation (Behr & Becker, 2018; Brizzi et al., 2021; Munch, 2020; Sobolev & Brown, 2019).

Understanding the main processes and their dynamic feedbacks, which influence upper plate extension and shortening, and the vertical motions of forearc and back-arc sedimentary basins during oceanic subduction and subsequent continental collision requires an integrated approach involving a high-resolution, coupled thermo-mechanical model handling elasto-visco-plastic rheologies of the crust and mantle and simulating erosion, sedimentation, and topographic evolution. In this study, we aim to quantify forearc and back-arc basin forming mechanisms and their subsidence history during oceanic subduction and subsequent continental collision by means of numerical forward modeling, constrained by observational data from the Carpathians, Calabrian, and Gibraltar subduction zones within the Mediterranean region (Figure 2). We conducted a parametric study testing systematically the influence of upper plate rheological weak zones, the role of different kinematic conditions, and different sedimentation rates on upper plate deformation and topographic evolution in distinct forearc and back-arc depocenters.

The Mediterranean region is an ideal area for understanding the formation and evolution of forearc – back-arc basin systems and their subsidence history due to the availability of high-resolution observational data of the subduction zones and sedimentary basins formed during slow plate convergence in a land-locked frame (e.g., Le Pichon, 1982, Figure 2). Sedimentary basins, such as the Pannonian-Transylvanian, Tyrrhenian-Paola, Western and Eastern Alboran, North and South Aegean basins formed in response to the retreat of the Carpathian, Ionian, Gibraltar, and Hellenic slabs during the formation of the Carpathians, Apennines, Betics-Rif and Hellenides orogens, respectively (e.g., d'Acremont et al., 2020; Faccenna et al., 2014; Horváth et al., 2015; Jolivet et al., 2009; Royden et al., 1982; Vergés & Fernàndez, 2012). In all cases, an extension was preceded by contraction and nappe stacking, and thus, extension affected a thick and hot orogenic crust, often reactivated weak thrust and suture zone segments, and exhumed previously buried rocks. Such weak zones are recognized today at the basin margins, localizing the oldest extensional deformation and forming major detachments of metamorphic core complexes (Brun & Faccenna, 2008; Brun & Sokoutis, 2010; Ustaszewski et al., 2010). The Mediterranean region also offers reliable kinematic constraints on subduction evolution based on available paleomagnetic and field studies (e.g., le Breton et al., 2021; Csontos & Vörös, 2004; van Hinsbergen et al., 2020), seismological, seismic and well data (Minelli & Faccenna, 2010; Rosenbaum & Lister, 2004; Spakman & Wortel, 2004; Villasenor et al., 2015; Wortel & Spakman, 2000) and based on absolute age dating (e.g., Faccenna et al., 2014; Lukacs et al., 2018 and references therein). These studies have shown that the convergence velocity of these systems was rather slow, that is,

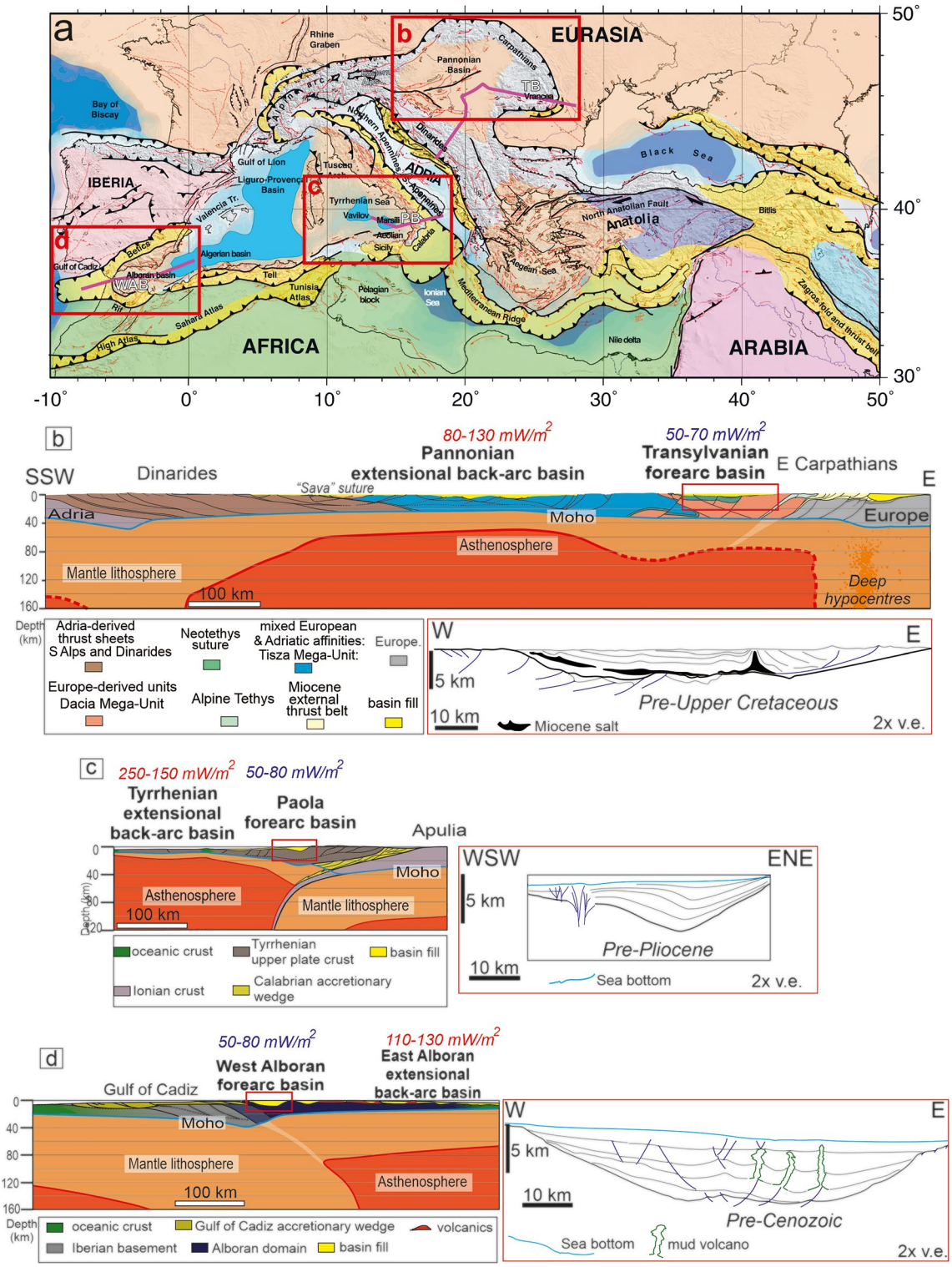

Figure 2. (a) Tectonic map of the Mediterranean (after Faccenna et al., 2014). Lithospheric-scale cross-sections and line drawing interpretation of seismic sections from the Transylvanian-Pannonian Basins (compiled after Balázs et al., 2018; Horváth et al., 2015; Krezsek et al., 2006; Matenco & Radivojević, 2012; Schmid et al., 2008; Tari et al., 1999; Tilita et al., 2013), Paola-Tyrrhenian Basins (compiled after Corradino et al., 2020; Minelli & Faccenna, 2010; Pepe et al., 2010; Zito et al., 2003) and Western and Eastern Alboran Basins (compiled after d'Acremont et al., 2020; Comas et al., 1999; Do Cuoto et al., 2016; Jimenez-Munt et al., 2019; Medialdea et al., 2004). Note the wide syncline structure of the similar retro-forearc basins having 50–80 mW/m^2 surface heat flow and the extended back-arc basins having thinned crust and high heat flow.

Table 1
Main Parameters of the Numerical Models

	Upper cont. crust	Lower cont. crust	Lithospheric mantle	Basalt	Gabbro	Weak zone	Sediments
Thickness (km)	20	15	75	3	5	-	varies
Rheology	wet quartzite	plagioclase	dry olivine	plagioclase	plagioclase	wet olivine	wet quartzite
Density, ρ_0 (kg m^{-3})	2,750	3,000	3,300	3,000	3,000	3,200	2,600
Pre-exponential factor, $1/A_D$ (Pa^n s)	1.97×10^{17}	4.8×10^{22}	3.98×10^{16}	4.8×10^{22}	4.8×10^{22}	5.0×10^{20}	1.97×10^{17}
Activation energy, E (kJ mol^{-1})	154	238	532	238	238	470	154
Power law exponent, n	2.3	3.2	3.5	3.2	3.2	4.0	2.3
Cohesion (Pa)	3×10^6	3×10^6	3×10^6	3×10^6	3×10^6	3×10^6	3×10^6
Coefficient of friction, sin(φ)	0.3–0.1	0.3–0.1	0.6–0.3	0.1	0.3–0.1	0.1	0.1
Radioactive heat production, H_r (μW/m^3)	2	0.2	0.022	0.022	0.024	0.022	2

Note. The rheological rock properties are adapted from previous studies (e.g., Balazs, Faccenna, et al., 2021; Gerya & Meilick, 2011; Gerya & Yuen, 2007).

0.5–2 cm/yr. Therefore, the subduction velocity (i.e., the sum of the back-arc motion or trench retreat and the plate convergence velocity) was mainly driven by variations of trench retreat (Dewey et al., 1989; Jolivet et al., 2009). Despite the similarities of these Mediterranean subduction zones, they show different amounts and rates of upper and lower plate velocities and different lengths of oceanic or continental slabs that resulted in different amounts of upper plate extension values, followed by a tectonic inversion. Our model setups are based on observational data and reconstructions from these Mediterranean subduction zones.

2. Method

2.1. Numerical Method Description

The 2D numerical models are conducted with the thermomechanical code I2ELVIS, which solves the mass, momentum, and energy conservation equations on an Eularian staggered grid, using finite differences and marker-in-cell techniques (Gerya & Yuen, 2007). Solving the energy equation including latent, adiabatic, radiogenic and shear heat production simulates the thermal evolution of the model. Physical properties are transported by Lagrangian markers that move with the velocity field interpolated from the fix grid. The code uses non-Newtonian elasto-visco-plastic rock rheologies (Table 1) and models in a simplified manner aqueous fluid transport and hydration/dehydration processes (for details see Supporting Information S1).

Surface processes, such as erosion and sedimentation are simulated at each time-step by the following transport equation:

$$\frac{\partial y_{\text{surf}}}{\partial t} = v_y - v_x \frac{\partial y_{\text{surf}}}{\partial x} - v_{\text{sedim}} + v_{\text{erosion}}$$

where t is time, y_{surf} is the vertical position of the surface as a function of the horizontal distance: x, v_y, and v_x are the vertical and horizontal components of the material velocity vector of the surface, v_{sedim} and v_{erosion} are the sedimentation and erosion rates, respectively (Gerya & Yuen, 2007; Gorczyk et al., 2007). Building on previous similar models (Gorczyk et al., 2007; Vogt et al., 2012) we show model results where partial melting is also considered (Modmelt in Table 2 and Figure S1 in Supporting Information S1). A more detailed description of the numerical approach is available in Gerya (2010) and in Supporting Information S1.

2.2. Model Setup

The models simulate horizontally forced subduction of an oceanic plate beneath a continental margin on a lithospheric to upper mantle cross-section sized 4,000 × 720 km^2. The rectangular grid of 1,361 × 283 nodal points is non-uniform and contains a 1,000 km wide high-resolution area of 1 × 1 km^2 in the center of the domain that gradually changes to 10 × 10 km^2 toward the model sides (Figure 2). The downgoing plate is built up by an oceanic and continental lithosphere connected by a 150 km wide passive margin. This passive margin length fits

Table 2
2D Model Parameter Tests

Numerical models	Ocean length	Sedimentation rate	Upper plate WZ & location	Boundary condition	Boundary condition duration	Effect on fore-arc & backarc evolution
1. ModRef	1,000 km	0.1 km/Myr	Hydrated mantle; 490 km	$V_l = 1.5$ cm/yr	Entire model run	Reference model
2. ModShort	550 km	0.1 km/Myr	Hydrated mantle; 490 km	$V_l = 1.5$ cm/yr	Entire model run	Intra-continental back-arc rift
3. ModLong	1,250 km	0.1 km/Myr	Hydrated mantle; 490 km	$V_l = 1.5$ cm/yr	Entire model run	Wide back-arc ocean
4. ModWZ330	1,000 km	0.1 km/Myr	Hydrated mantle; 330 km	$V_l = 1.5$ cm/yr	Entire model run	Arc-rifting
5. ModWZ690	1,000 km	0.1 km/Myr	Hydrated mantle; 690 km	$V_l = 1.5$ cm/yr	Entire model run	Enhanced back-arc rifting
6. ModWZ1050	1,000 km	0.1 km/Myr	Hydrated mantle; 1050 km	$V_l = 1.5$ cm/yr	Entire model run	Distal & lower back-arc deformation rates
7. ModHolon	1,250 km	0.1 km/Myr	none	$V_l = 1.5$ cm/yr	Entire model run	No back-arc deformation
8. ModHolonts	1,250 km	0.1 km/Myr	none	$V_l = 1.0$, $V_l = 0.5$ cm/yr	Entire model run	No back-arc deformation
9. Modmelt	550 km	0.1 km/Myr	Volcanic arc	$V_l = 1.5$ cm/yr	Entire model run	Lower initial forearc subsidence, then arc rifting
10. Modcr	550 km	0.1 km/Myr	Hydrated mantle and crustal WZ, 490 km	$V_l = 1.5$ cm/yr	Entire model run	Localized and earlier back-arc deformation
11. ModShorthot	550 km	0.1 km/Myr	Hydrated mantle; 490 km and higher T_{moho}	$V_l = 1.5$ cm/yr	Entire model run	Enhanced slab roll-back & earlier back-arc rifting
12. ModShorthom	550 km	0.1 km/Myr	none	$V_l = 1.5$ cm/yr	Entire model run	No back-arc deformation
13. ModRes (600 m resolution)	1,000 km	0.1 km/Myr	Hydrated mantle; 490 km	$V_l = 1.5$ cm/yr	Entire model run	High resolution model
14. Modfre	550 km	0.1 km/Myr	Hydrated mantle, 490 km	$V_l = 1.5$ cm/yr	Until 36 Myr	Retreating slab, back-arc rifting, forearc uplift
15. Modtw	550 km	0.1 km/Myr	Hydrated mantle, 490 km	$V_l = V_u = 0.75$ cm/yr	Entire model run	Lower slab dip, lower forearc subsidence
16. Modtwfr	550 km	0.1 km/Myr	Hydrated mantle, 490 km	$V_l = V_u = 0.75$ cm/yr	Until 36 Myr	Slab steepening and forearc subsidence during free-fall subduction
17. Modwzrev	550 km	0.1 km/Myr	Hydrated mantle,490 km	$V_u = 1.5$ cm/yr	Entire model run	Lowest slab dip and forearc subsidence and suppressed back-arc rifting
18. Modlosed	1,000 km	0.05 km/Myr	none	$V_l = 1.5$ cm/yr	Entire model run	Higher stress accumulation and subsidence values
19. Modhised	1,000 km	0.5 km/Myr	none	$V_l = 1.5$ cm/yr	Entire model run	Lower stress accumulation and subsidence values
20. Modlosedfr	1,000 km	0.05 km/Myr	none	$V_l = 1.5$ cm/yr	Until 30 Myr	Highest subduction velocity and high dynamic subsidence
21. Modhisedfr	1,000 km	0.5 km/Myr	none	$V_l = 1.5$ cm/yr	Until 30 Myr	Lower subduction velocity and lower dynamic subsidence
22. Modlosedfrup	1,000 km	0.05 km/Myr	none	$V_u = 1.5$ cm/yr	Until 32 Myr	High subduction velocity and high dynamic subsidence
23. Modhisedfrup	1,000 km	0.5 km/Myr	none	$V_u = 1.5$ cm/yr	Until 32 Myr	Lower subduction velocity and upper plate tilting

Note. In a visco-plastic experiment (Modmelt) melt extraction is implemented and the development of a volcanic arc is simulated. Further model results are shown in Supporting Information S1.

well with observational data from modern analogs (e.g., Jolivet et al., 2018). The width of the oceanic domain is varied in a series of models between 550, 1,000, and 1250 km. The continental crust consists of a 20 km upper crust (wet quartzite rheology) and a further 15 km lower crust (plagioclase rheology) defining average values (e.g., Tesauro et al., 2009). The overriding continent also hosts a 275 km wide orogenic area of increased upper and lower crustal thickness of 21 and 18 km, respectively. Furthermore, underneath this orogenic segment, an inclined weak zone of wet olivine rheology is defined in the lithospheric mantle, representing an inherited

suture zone (Figure 3). Simulating a thick crust and a hot and heterogenous lithosphere agrees with geological constraints on back-arc lithospheric extension and has been also inferred and applied in previous studies (e.g., Balazs, Maţenco, et al., 2021; Fodor et al., 2021; Horvath et al., 2015; Sokoutis et al., 2007). The role of different upper plate weak zones and their distance from the trench is assessed in parameter tests. The oceanic crust is represented by 3 km basalt and a further 5 km gabbroic crust. Both the lithospheric and the sub-lithospheric mantle are composed of anhydrous peridotite (dry olivine rheology). An inclined weak zone defined by low plastic strength and wet olivine rheology is placed along the active margin to initiate subduction (Figure 2).

Free slip boundary condition is defined on all model sides. 20 km sticky air is defined on top of the model to simulate an internal free erosion/sedimentation surface (cf., Crameri et al., 2012). The sedimentation rate is varied in a series of experiments between 0 and 0.5 km/Myr. In order to initiate subduction, a horizontal velocity condition of 1.5 cm/yr is defined on the lower plate or on both plates. This boundary condition is kept constant in a series of models or turned off in another series of experiments after the slab reaches ca. 350 km depth. Therefore, we compared models with the slow and constant convergence that is in the best agreement with Mediterranean constraints (Jolivet et al., 2009) with models where both the subduction and convergence velocity is solely driven by the forces within the system. In another series of experiments, the velocity boundary condition is set to 0 during the continental collision stage. The initial thermal properties of the left and right continents are horizontally uniform reaching 0°C on the surface, 645°C at Moho depth, and 1300°C at 110 km depth representing the base of the lithosphere. This moderately high Moho temperature characterizes young orogenic areas, prior to their extensional collapse well-representing pre-rift back-arc values (e.g., Brun & Sokoutis, 2010; Diaferia et al., 2019; Jolivet et al., 2018). The thermal structure of the ocean is defined using a half-space cooling model with uniform oceanic plate age of 50 Myr. The asthenospheric mantle is characterized by an initial adiabatic temperature gradient of 0.5°C/km. Our applied rheological and thermal values are like values from geological reconstructions of the Mediterranean region prior to back-arc extension (Faccenna et al., 2014). Further models analyzing the influence of different rheological layering and initial temperature profiles are shown in Supporting Information S1. Model results are visualized by rock composition, effective viscosity, and subsidence evolution. Furthermore, we show the magnitude of the horizontal component of the deviatoric stress tensor ($\sigma_{xx} = -\sigma_{zz}$) and the orientation of the principal stresses (Figures 4–11).

3. Results

All our models evolve in four distinct stages associated with specific tectonic processes and mantle flow patterns. *Stage 1: forced subduction initiation and incipient subduction* along a former passive margin governed by far-field compression (e.g., Toth & Gurnis, 1998) leading to the initial underthrusting of the oceanic plate beneath the continental margin and associated upper crustal deformation. *Stage 2: mature oceanic subduction* showing the gradual consumption of the oceanic lithosphere, slab steepening, and gradually increasing the strength of the poloidal mantle flow velocity. *Stage 3: soft collision and onset of continental subduction* marking the subduction of the extended continental passive margin of the lower plate. *Stage 4: hard collision* is associated with the arrival of the unextended continental lithosphere into the subduction zone leading to upper crustal subduction and subsequent exhumation and orogenic build-up preceding slab break-off. All the models show the evolution of a forearc topographic high and a topographic depression in the upper plate overlying the subduction interface and the mantle wedge. Furthermore, surface subsidence is simulated during crustal thinning at larger distances from the forearc depression on the overriding plate controlled by crustal thinning. In the following we classify the topographic depression above the subduction interface to be a retro-forearc basin and the more distal depression as a back-arc basin.

Every model simulates the subduction of the hydrated oceanic crust and sediments into the upper mantle where dehydration takes place. Fluids are released from the slab and hydrate the subduction interface and the overlying lithosphere, while the influence of melts and the formation of a volcanic arc is simulated in other experiments (Figure S1 in Supporting Information S1).

3.1. Reference Model

The reference model (see Movies S1–S6) includes the 1,000 km wide oceanic basin and a constant 1.5 cm/yr convergence velocity condition imposed on the lower plate, while the upper plate is fixed. The subduction

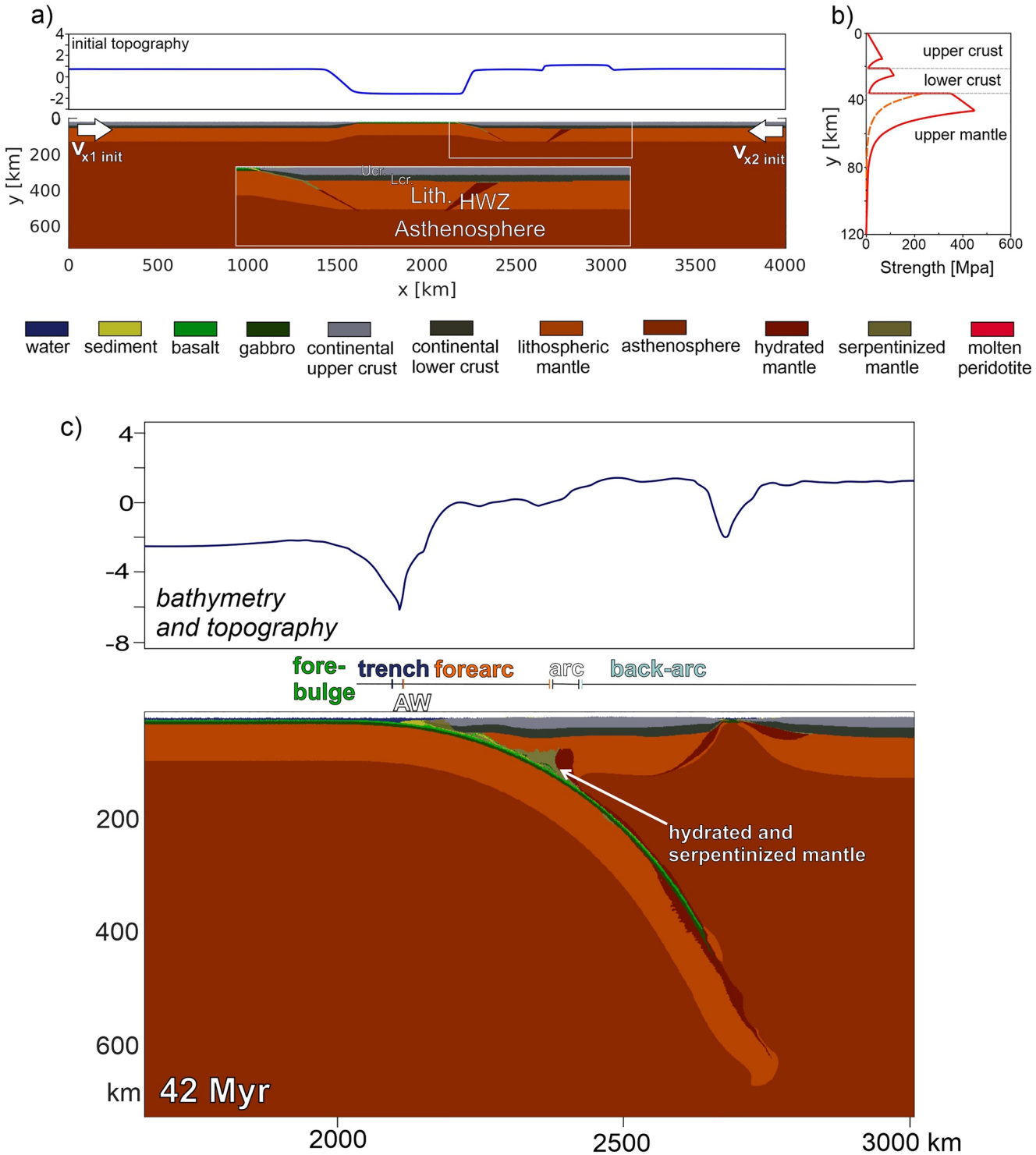

Figure 3. Initial model setup. (a) 2D domain is resolved by 1361 × 283 nodal points, with more than 7 million randomly distributed markers. The model domain consists of a continental overriding plate and a subducting plate including both oceanic and continental lithosphere. An inclined weak zone of wet olivine rheology is defined along one edge of the ocean to initiate subduction. Additional hydrated weak zone (HWZ) is defined in the overriding plate representing an inherited suture zone. (b) Initial strength profile of the continental overriding plate (assuming constant strain rate of 10^{-14} s^{-1}). Red line indicates the laterally homogenous lithosphere, orange dashed line corresponds to the hydrated weaker lithosphere. (c) Rock composition and topography model result of the reference model indicating the location and bathymetry of the trench, the accretionary wedge (AW), forearc and back-arc domains discussed in the text.

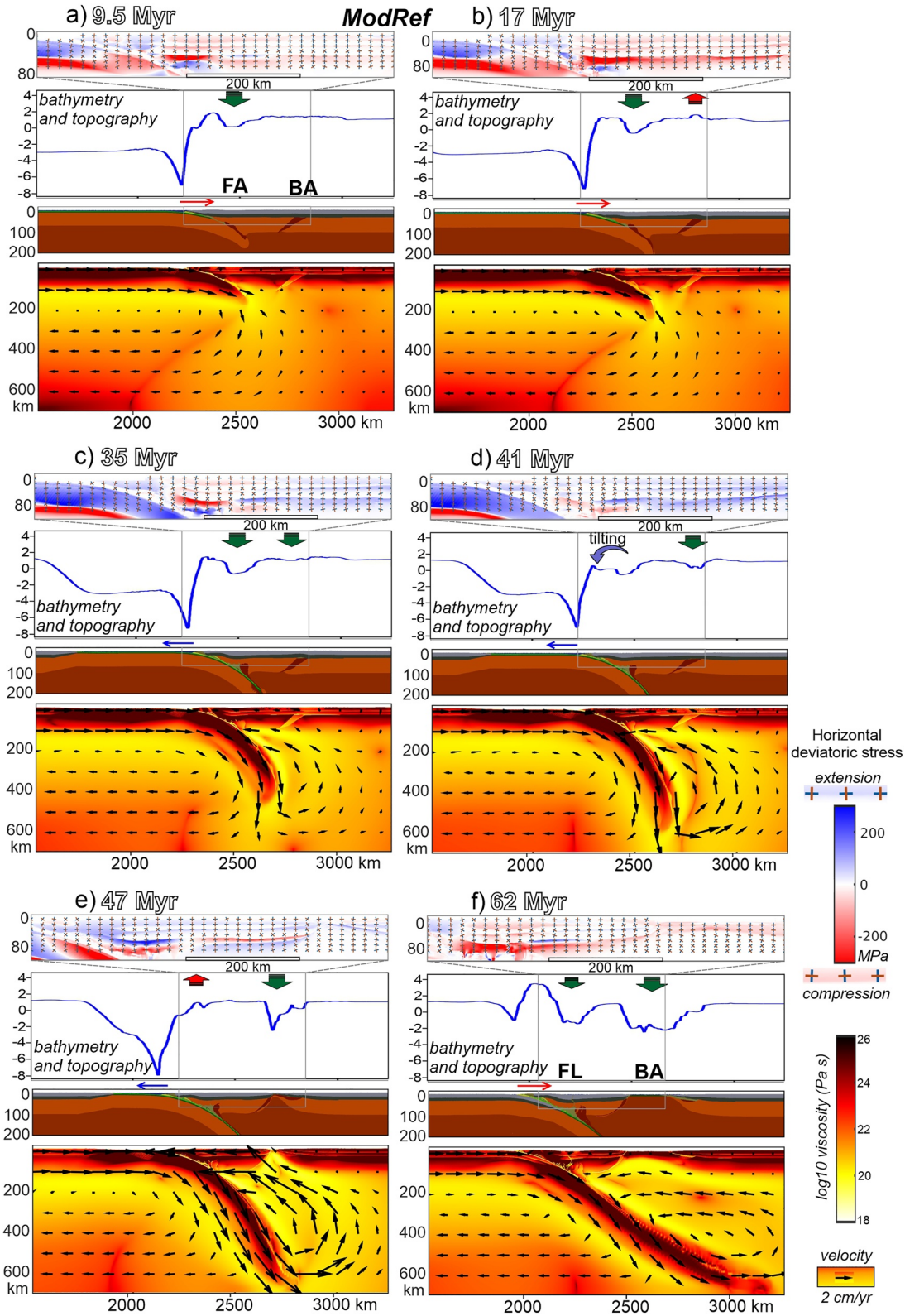

Figure 4. (a–f) Evolution of the reference model (*ModRef*) shown by topography, effective viscosity sections overlain by velocity vectors, rock composition, horizontal deviatoric stress (σ_{xx}) and orientation of the principal stresses in the center of the model. FA – forearc domain, BA – back-arc domain, FL – (retro-)foreland basin. Green and red arrows over the topography plots indicate subsidence and uplift, respectively, in the forearc and back-arc domains at different stages. Blue and red arrows over the rock composition figures indicate trench retreat and advance, respectively. Subsidence curve of the reference model is shown in Figure 5.

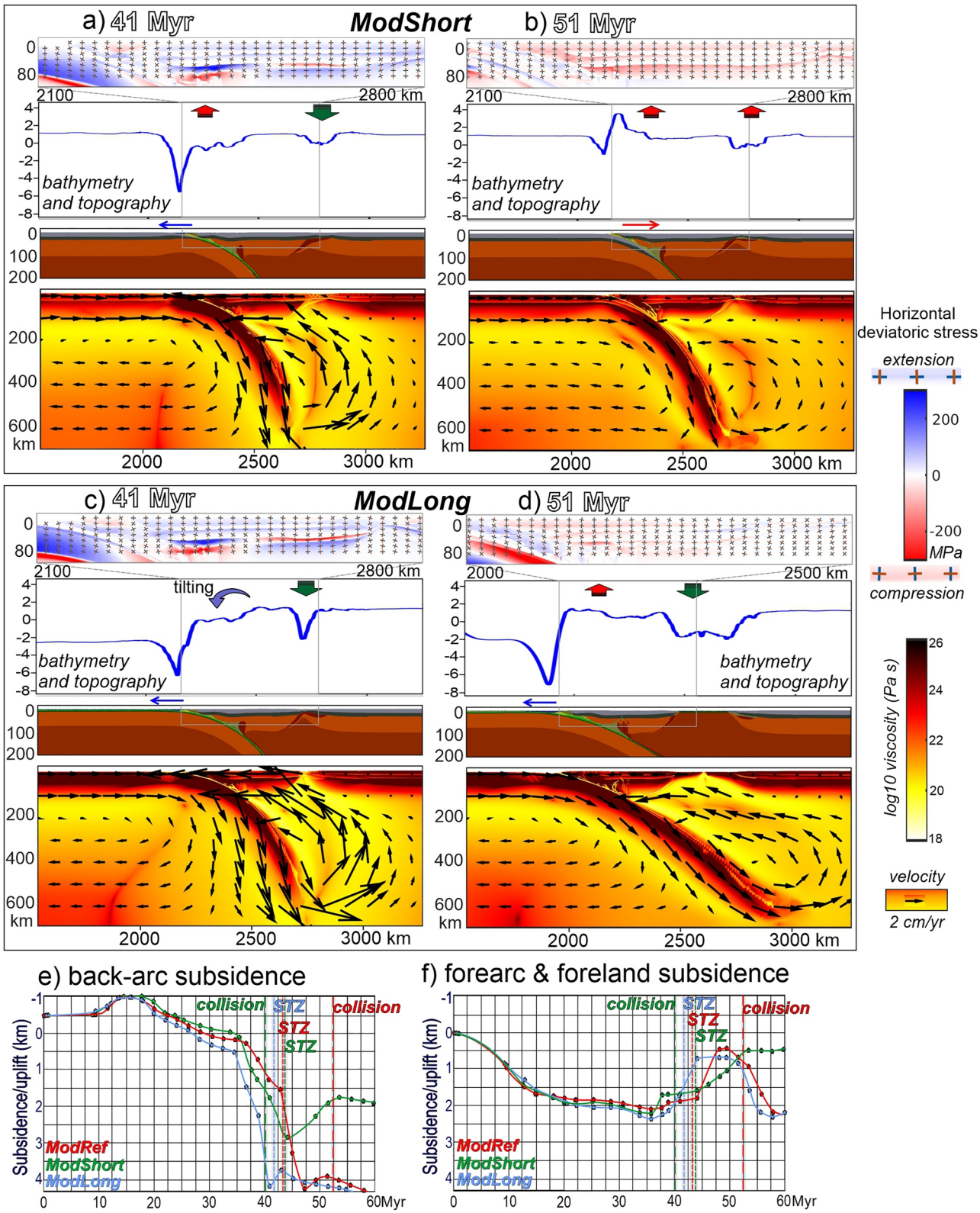

Figure 5. Evolution of the models including a 550 km wide (*Modshort*) and a 1,250 km wide (*ModLong*) oceanic lower plate showing topography, effective viscosity sections overlain by velocity vectors, rock composition, horizontal deviatoric stress (σ_{xx}) and orientation of the principal stresses in the center of the model. Green and red arrows over the topography plots indicate subsidence and uplift, respectively. Blue and red arrows over the rock composition figures indicate trench retreat and advance, respectively. (e–f) Long-term subsidence history of the forearc and back-arc regions. STZ – onset of slab transition zone interaction.

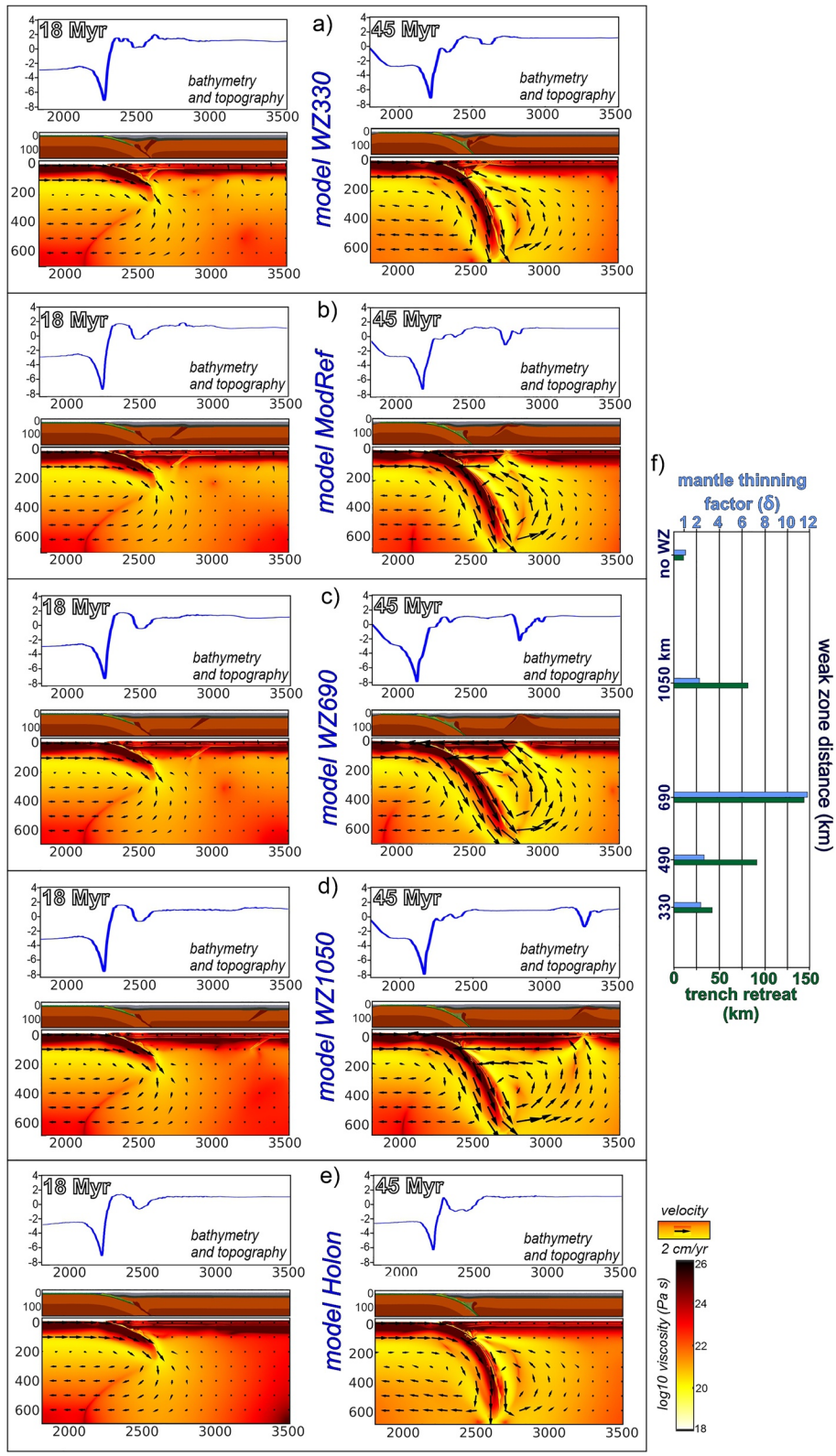

Figure 6. Parameter test on the influence of different weak zone locations. (a–e) Topography, rock composition and effective viscosity results of the models. (f) Plot shows the trench retreat and back-arc mantle thinning values reached after 45 Myr in the models.

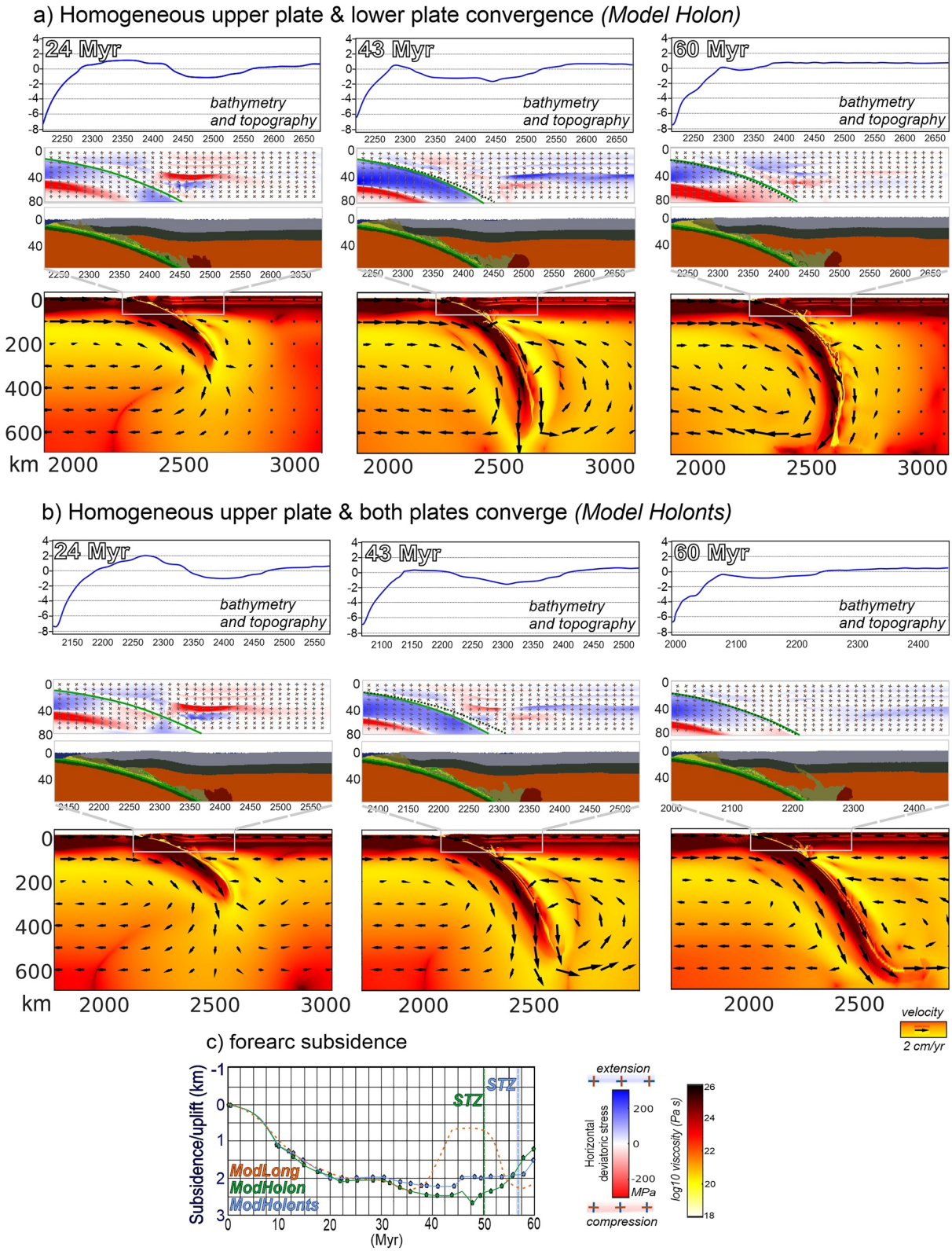

Figure 7. Comparison of model results with homogenous upper plates, 1,250 km wide oceanic lower plates and different convergence velocities applied (a) only on the lower plate or (b) distributed between the lower and upper plates. Subduction interface is highlighted by continuous green lines overlying the stress field figures. Dashed green line indicates the subduction interface position at 24 Myr. Note the gradual slab steepening. (c) Forearc subsidence history was extracted from these two models. Dashed orange line shows the subsidence of the forearc basin from the model with an upper plate weak zone (*ModLong*).

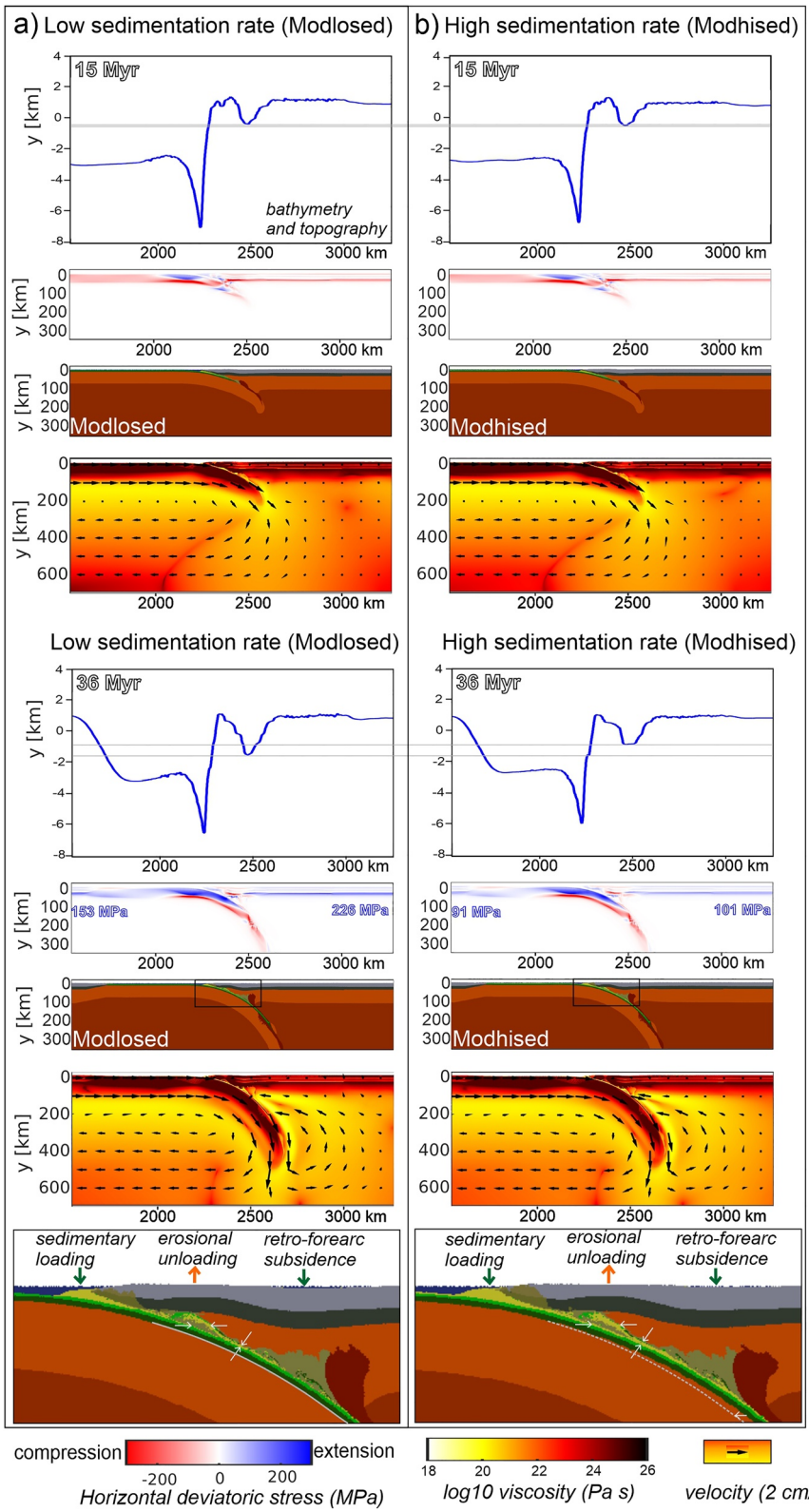

Figure 8. Parameter test on the influence of different erosion and sedimentation rates. Constant velocity condition is imposed on the lower plate. Note that thicker sediment accumulation results in a weaker subduction interface and less efficient stress transfer toward the upper plate and lower forearc basin subsidence. Furthermore, higher erosion and sedimentation rates lead to a shallower dipping slab. Dashed white line in the compositional figure with higher sedimentation rate shows the slab geometry of *Modlosed*.

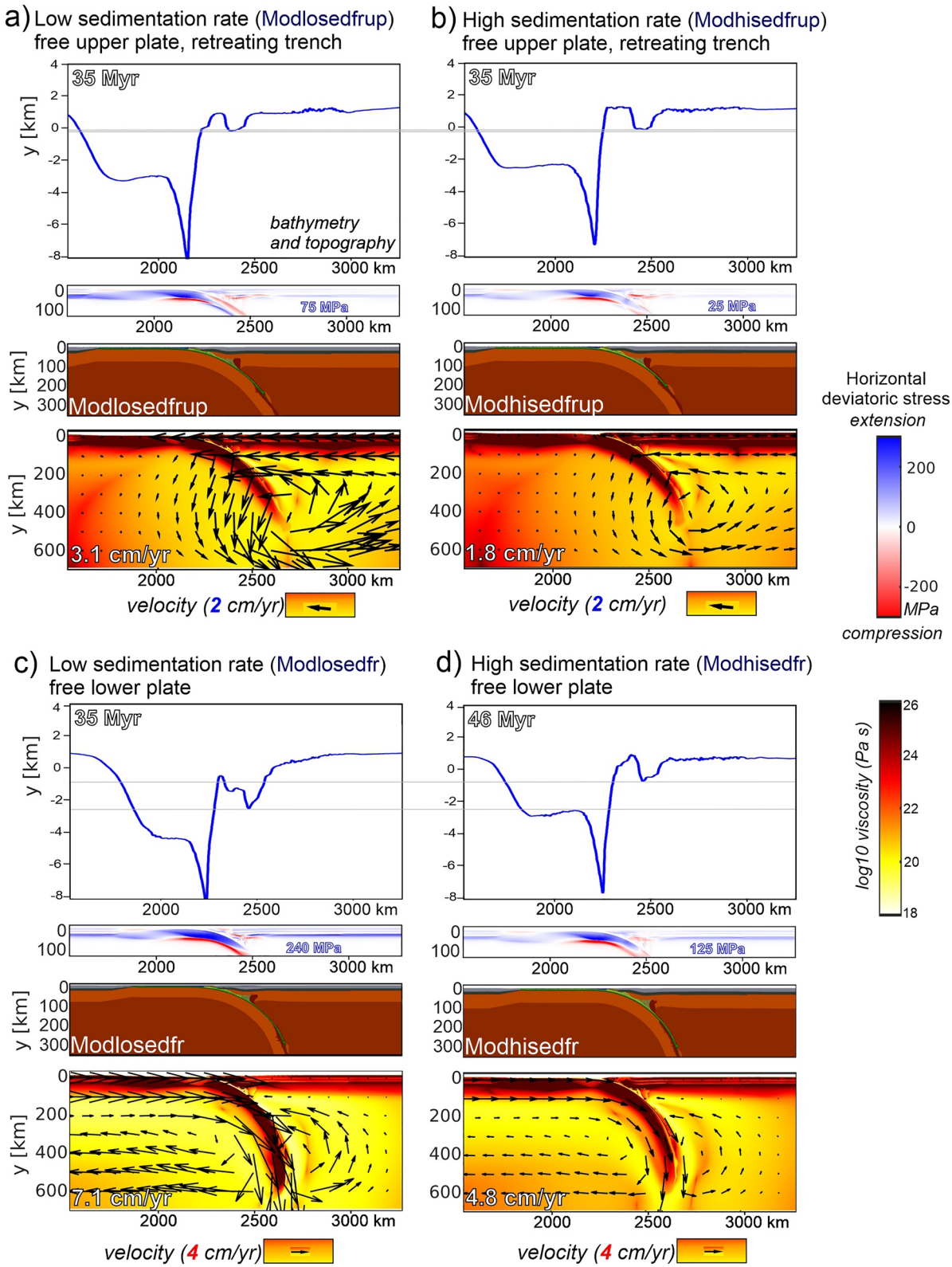

Figure 9. Parameter test on the influence of different erosion and sedimentation rates and convergence kinematics. No velocity boundary conditions are imposed after the slab reaches 380 km depth. (a) Free upper and fixed lower plate and lower sedimentation rate. (b) Free upper and fixed lower plate and higher sedimentation rate. (c) Fixed upper and free lower plate and lower sedimentation rate. (d) Fixed upper and free lower plate and higher sedimentation rate. Higher subduction velocity is reached in the experiment with lower sedimentation and erosion rates. Note the different scales of the velocity vectors.

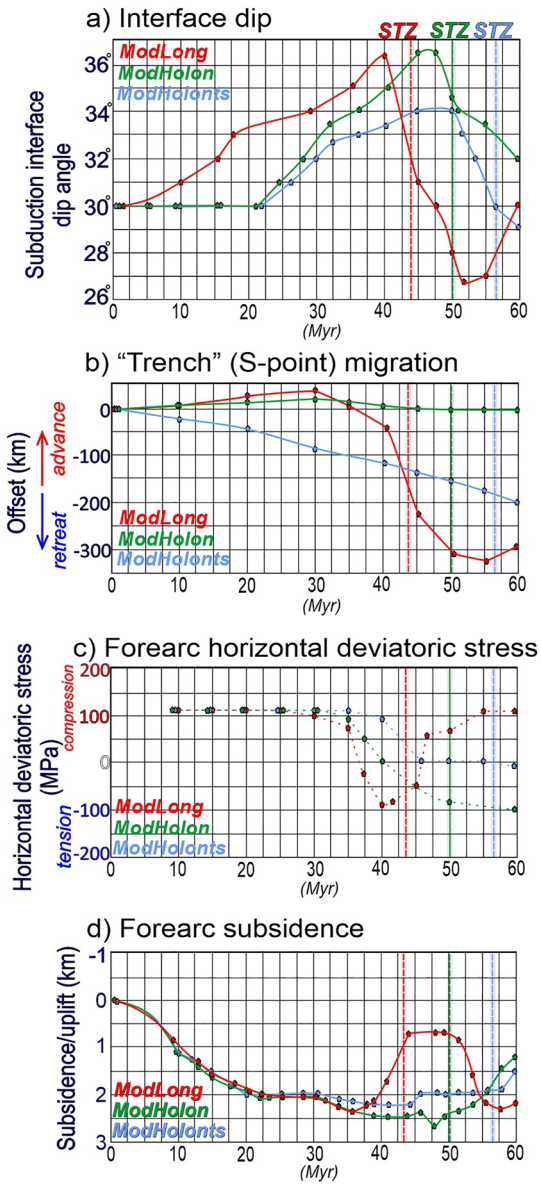

Figure 10. Comparison of the evolution of different model attributes, that are extracted from three models (Table 2) with the 1,250 km oceanic lower plates. (a) Subduction interface dip angle measured at the base of the upper plate lithosphere. (b) Horizontal position of the contact point of the upper and lower plate (S-point). (c) Maximum value of the horizontal deviatoric stress measured in the crust. (d) Subsidence of the forearc depocenter. STZ – slab transition zone interaction.

velocity evolves as a sum of the convergence and slab retreat velocities driven by the forces within system. A hydrated weak zone is placed in the mantle at 490 km horizontal distance from the trench (Figure 4). Such a zone and the overlying 39 km thick crust imitate the pre-rift structural inheritance of the back-arc domain as inferred by observational data from the Mediterranean (e.g., Brun & Sokoutis, 2010; Diaferia et al., 2019; Jolivet et al., 2018; Ustaszewski et al., 2010).

During stage 1 subduction initiation and incipient subduction and the first 17 Myr of convergence, show slow trench advance and compressional stress accumulation in the upper plate (Figures 4a and 4b). Sediments are deposited in the ca. 7 km deep trench forming an accretionary wedge (yellow color in rock composition figures). Subduction initiation, underthrusting of the oceanic lithosphere, and incipient subduction lead to brittle deformation of the forearc domain resulting in a series of low offset normal and reverse faults during the first 10 Myr. A pronounced forearc high and a topographic depression is formed on the upper plate showing a forearc syncline structure. The depocenter of this syncline is located at ca. 200 km distance from the accretionary wedge overlying the subduction interface. The average subsidence for this first 10 Myr is 1 km in the retro-forearc domain, followed by a monotonous additional 1 km subsidence until 20 Myr. The area above the distal mantle weak zone is uplifted due to contractional strain localization and further crustal thickening (Figures 4a and 4b).

Trench advance is switched to trench retreat during stage 2 (Figures 4c–4e). The mantle return flow velocity gradually increases and the accretionary wedge thickens. By 35 Myr the back-arc of the upper plate is under extension (blue color in σ_{xx} figures), while the forearc still records compressional horizontal stress (red color in σ_{xx} figure; Figure 4c). Maximum subsidence of the retro-forearc syncline structure is reached after 35 Myr, followed by its slow uplift from 37.5 Myr (Figures 4c and 4d). The former forearc high records subsidence and eventually the upper plate gets tilted toward the trench, resulting in the trench-ward shift of the depocenter location between the accretionary wedge and the former forearc syncline (Figures 4d and 4e). By this time, the forearc compressional stress field changes to extension in the crust and upper lithosphere, while the base of the upper plate lithosphere is affected by suction from the underlying retreating slab (horizontal compression, vertical tension in Figures 4d and 4e). Furthermore, slab retreat is accommodated by upper plate extension. First, the back-arc crustal domain that previously localized contractional deformation and thickened during stage 1 (Figure 4b), undergoes negative tectonic inversion associated with crustal and lithospheric thinning and ca. 100 m/Myr subsidence (Figures 4b and 4c). The model shows the migration of extensional structures in the crust from the initial location of the weak zone toward its dip direction, while the inherited hydrated weak zone is gradually re-distributed at the base of the crust. This back-arc subsidence rate increases to ca. 200 m/Myr from 37 Myr (Figure 5e).

The leading edge of the slab reaches the 660 km lower boundary at ca. 42.5 Myr. It is followed by accelerated, ca. 200 m/Myr forearc uplift (Figures 4d and 4e). At this stage, slab roll-back, back-arc extension, and subsidence continue and back-arc rifting ultimately leads to break-up and back-arc spreading at ca. 48 Myr (Figure 4e). During these stages of back-arc continental rifting the slab roll-back velocity increases to 3 cm/yr and the back-arc subsidence rate reaches a maximum of 350–400 m/Myr (Figures 4e and 5e). During stage 3 and soft collision, that is, subduction of the thinned continental passive margin from 52 Myr, trench retreat and back-arc spreading continue. Finally, during stage 4 of hard collision, trench advance is observed from ca. 56 Myr linked to the

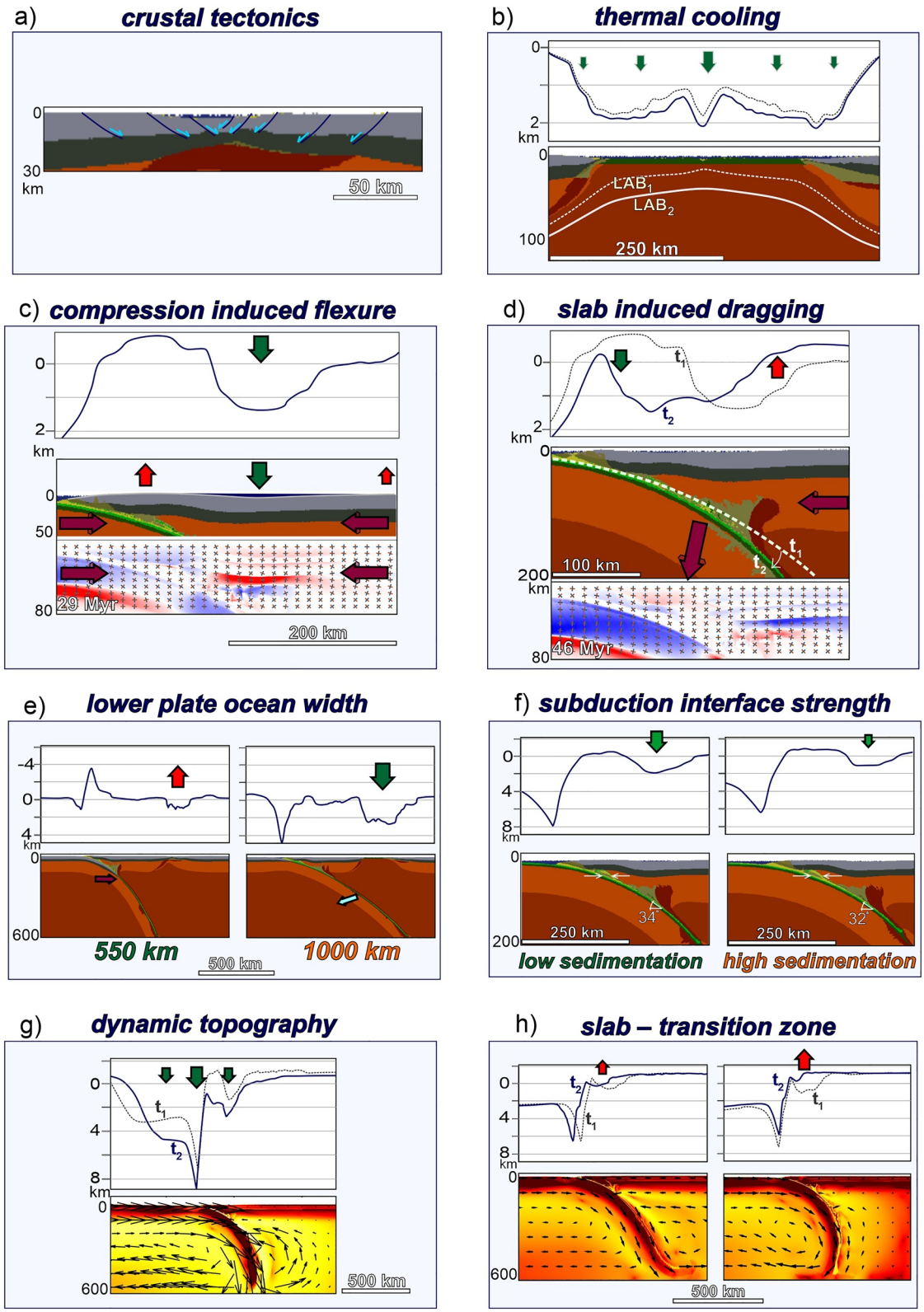
a) crustal tectonics
0
30
km
50 km
b) thermal cooling
0
2
km
0
LAB1
LAB2
100
250 km
c) compression induced flexure
0
2
km
0
50
80
29 Myr
200 km
d) slab induced dragging
0
t1
t2
km
2
0
100 km
t2
t1
200
km
46 Myr
80
e) lower plate ocean width
-4
0
4
km
0
600
550 km
500 km
1000 km
f) subduction interface strength
0
4
8
km
0
34
250 km
32
250 km
200
low sedimentation
high sedimentation
g) dynamic topography
0
t1
4
t2
8
km
0
600
500 km
h) slab – transition zone
0
t2
t1
4
t2
t1
8
km
0
600
500 km

Figure 11.

ongoing slow convergence (Figure 4f). Both the upper and lower plates record compression leading to the gradual build-up of a high orogenic structure, subsidence of a (retro-) foreland basin, and thermal subsidence and subduction initiation of the previously formed back-arc ocean (Figure 4f, Figure S2 in Supporting Information S1).

3.2. Sensitivity Analysis

We test the sensitivity of the reference model by varying its initial configuration, applying different kinematic conditions, modifying its rheology, and imposing different surface process rates.

3.2.1. The Role of Oceanic Basin Length

The reference model (Figure 4) is compared with two additional models having shorter, 550 km and wider, 1,250 km long oceanic basins (Figure 5). Modeling a longer oceanic lower plate allows the development of a greater slab-pull due to a long-lasting oceanic subduction stage prior to continental collision. Furthermore, comparing these three models allow the separation of the distinct effects of slab roll-back, slab transition zone interaction, and soft and hard collision on surface topography. All other parameters are kept the same as in the reference model including a hydrated mantle weak zone in the upper plate.

Stages 1 and 2 are similar in all three models Figures(4a–4cand5), but the longer oceanic subduction leads to higher trench retreat and thus higher upper plate extension values. This results in a crustal break-up after the distal back-arc rifting stage (Figures 4d and 5d). In contrast, in the shorter oceanic subduction model (Figures 5a and 5b) only back-arc continental rifting is reached, and extension switches to compression during a hard collision from 51 Myr (Figure 5b). Upper plate tilting and fore-arc uplift commence in all three models from ca. 37 Myr when the slab retreat velocity increases. In the case of *ModShort* (Figures 5a and 5b), a soft collision occurs from ca. 40 Myr prior to the leading edge of the slab reaching the bottom of the model. This stage corresponds with gradually increasing uplift rates of the trench and forearc domain, but the trench still retreats, and upper plate extension continues until the lower plate continental crust reaches ca. 100 km depth. Thereafter, during stage 4 of hard collision, the trench advances, leading to upper plate compression and positive structural inversion superimposed on the slow thermal subsidence of the previously formed extensional intra-continental back-arc basin (Figure 5b).

In the model with the longest oceanic lower plate (*ModLong*, Figures 5c and 5d) the slab rolls back and the trench retreats ca. 350 km until ca. 52 Myr resulting in a ca. 250 km wide back-arc ocean. The slab reaches the bottom of the model domain at ca. 42 Myr resulting in a rapidly decreasing slab dip angle. By 51 Myr, the subduction is shallow dipping (ca. 27 °), slab roll-back and trench retreat slow down and the ongoing slow convergence results in upper plate compression and retro-fore-arc subsidence again, while the back-arc ocean records slow thermal subsidence (Figures 5d and 5f).

3.2.2. The Role of Upper Plate Weak Zone Location

We present the influence of the upper plate weak zone horizontal distance from the trench (Table 2; Figure 6). In a series of models, the lithospheric weak zone is placed at 330, 490 (*ModRef*), 690, and 1,050 km distance from the trench. The overall model evolution is similar in these models, showing the initial flexural subsidence of the forearc depocenters and thereafter crustal and lithospheric thinning of the back-arc domain during slab roll-back and trench retreat that coincides with upper plate tilting and forearc uplift. The different weak zone locations, however, modify the timing and rates of back-arc extensional deformation. Earlier and fastest slab roll-back and related mantle flow and trench retreat velocities are reached when the weak zone is placed at a 690 km distance from the trench. In this model lithospheric break-up is reached by 45 Myr followed by 148 km trench retreat. When the weak zone is placed at a larger (1,050 km) or smaller (490) distance from the trench, its retreat value is only 80 and 85 km, respectively, resulting in lower mantle thinning values. In the case where the weak zone

Figure 11. Summary of the main crustal and mantle processes influencing forearc and back-arc basin subsidence and topography. (a) Rock composition of the extended back-arc domain. Crustal thinning and thickening lead to isostatic subsidence and uplift, respectively. (b) Thermal cooling of the back-arc mantle after the cessation of slab roll-back lead to regional slow subsidence. (c) Rock composition and stress field. Forearc compression (in red) leads to flexural subsidence. (d) Slab steepening during free-fall subduction drags down the overriding plate. Subsidence of the forearc high and upper plate trench-ward tilting is controlled by decreasing slab dip and related dragging. (e) Subduction of a shorter oceanic basin leads to moderate back-arc lithospheric extension, while a longer oceanic subduction history results in higher slab roll-back and extension values leading to crustal break-up. (f) Higher sedimentation leads to a shallower dipping slab, weaker interface, less efficient stress transfer and lower forearc subsidence. (g) Trench and upper plate dynamic subsidence driven by increased mantle convection velocity and related vertical stresses. (h) Forearc uplift driven by the interaction of the slab with the bottom of the upper mantle.

is placed in the position closest location to the subduction zone (Figure 6a, model *WZ330*), the initial trench advance value is higher, most of the contractional deformation is localized above the weak zone and the initial forearc depocenter depth is somewhat lower, reaching only 1,400 m until 18 Myr. The amount of subsequent trench retreat is smaller, reaching only 80 km until 45 Myr (Figure 6f).

3.2.3. The Role of Convergence Kinematics

All these previous models included weakness zones in the upper plate and showed gradually increasing subduction velocities that were driven by the increasing slab roll-back velocities and accommodated by upper plate extension. To separate the influence of upper plate extension from other processes on forearc topographic evolution, we conducted a series of models with strong and homogenous upper plates, effectively suppressing trench advance and retreat values (Figures 6e and 7). Furthermore, we compare this evolution with a similar model, where the same 1.5 cm/yr constant plate convergence velocity is distributed between the lower and upper plates (Figure 7b). In the latter model (*ModHolonts*), the slab dip angle is expectedly lower (cf., van Hunen et al., 2000, 2004) and the subduction curvature radius is larger compared to the model where only the lower plate is pushed (*ModHolon* in Figure 7a).

In the model where no upper plate weak zones are present (Figures 6e and 6f) the value of the initial trench advance is only 67% of the reference model advance (Figure 4). The initial compression induced forearc subsidence is similar in all these models (Figure 7c). Thereafter, during stage 2, upper plate compression gradually changes to extension and the models show gradual slab steepening before the leading edge of the slab reaches the lower model boundary. In these models having a strong homogeneous upper plate (Figure 7), the trench retreat value is suppressed and reaches only ca. 20–30 km. The reference model by 43 Myr showed rapid slab retreat, upper plate tilting, and forearc uplift (Figure 4), while in the models with strong homogenous upper plates, forearc subsidence continues during stage 2. This subsidence is superimposed on the tilting of the upper plate and subsidence of the forearc high (Figure 7). *ModHolon* shows ca. 75 MPa extensional stress in the forearc crust and subcrustal lithospheric mantle and vertical tension (horizontal compression) at the base of the overriding plate, implying the vertical dragging by the lower plate (Figure 7). *Modholon* shows a steeper slab geometry as its leading edge sinks deeper, which contributes to higher values of extensional stress accumulation in the upper plate. Its forearc subsidence value is 320 m larger than in the model where both the upper and lower plates are pushed (Figure 7). From 47 Myr, in *ModHolon*, the leading edge of the slab reaches the bottom of the model at a high angle which leads to the backward bending of the slab and the high rate of uplift of the forearc (Figure 7a). While in this case, when both the upper and lower plates were pushed (Figure 7b) and the slab dip angle is lower, the slab lays onto the lower boundary and the modeled forearc uplift rate is lower (Figure 7c, Figure S3 in Supporting Information S1).

In the model (*ModCr*), where both crustal and mantle weak zones are present and thus, the upper plate is weaker than in the reference model, higher initial trench advance and higher subsequent trench retreat values are simulated than in the reference model and upper plate extensional deformation is localized along this weak zone (Figure S4 in Supporting Information S1).

3.2.4. The Role of Free-Fall Subduction and Surface Processes

We evaluate the influence of upper plate and lower plate velocity conditions and their temporal variations. Additionally, we analyzed the role of different erosion and sedimentation rates on the upper plate topographic evolution (Figures 8 and 9). These parameters are assessed by six simulations, where the upper plate is kept homogenous, and a 1,000 km long oceanic basin is used. In two models (*Modlosed* and *Modhised*) a constant 1.5 cm/yr velocity is imposed on the lower plate throughout the entire model run (Figure 8). Stage 1 of incipient subduction is similar to the reference model in the models with lower and higher sedimentation rates. Compressional stress is accumulated in the upper plate and the retro-forearc basin records ca. 1.75 km subsidence. In *Modhised* by 36 Myr of subduction a much thicker accretionary wedge developed in the subduction zone, furthermore, the subducted sediments are underplated below the forearc high and are further subducted within the subduction interface having a notably greater thickness (Figure 8). The retro-forearc basin subsidence in the models with lower and higher sedimentation rates is 2.4 and 1.8 km, respectively. The model with higher sedimentation rate also shows a shallower dipping subduction zone compared to the model with lower sedimentation rates (Figure 8). Furthermore, the accumulated extensional stress in the upper plate reaches ca. 200 MPa in the model with lower sedimentation, while this value is only 110 MPa in the models with higher sedimentation.

In four further models with lower and higher erosion rates, the boundary velocity condition is turned off after the leading edge of the slab is at ca. 380 km depth (Figure 9). In two models where the lower plate is fixed and the upper plate is free to move, this depth is reached at 32 Myr (Figures 9a and 9b). While in the models where the upper plate is fixed, the 380 km depth is reached after 30 Myr of model run (Figures 9c and 9d). Thereafter subduction velocity is solely determined by the dynamics and forces within the system.

In the models where the lower plate is fixed, the trench retreats with gradually increasing velocities associated with gradually increasing mantle flow velocities (Figures 9a and 9b). By 35 Myr, the trench retreat velocity in the model with lower surface processes rates (*Modlosedfrup*) reaches 3.1 cm/yr, while it only reaches 1.8 cm/yr in the model with higher surface processes rates (*Modhisedfrup*). The model with lower sedimentation shows a deeper trench and upper plate trench-ward tilting (Figures 9a and 9b).

In the upper plate fixed model with a lower sedimentation rate (*Modlosedfr*), the subduction velocity gradually increases from the initially pre-defined 1.5 cm/yr a maximum of 7.1 cm/yr by 35 Myr (Figure 9c). In this model with the highest slab roll-back velocity, larger dynamic subsidence is observed reaching a maximum of 3.2 km before the slab reaches the bottom of the model (Figure 9c). In the model with higher sedimentation rates (*Modhisedfr*), the subduction velocity increases to a maximum of 4.8 cm/yr by 46 Myr. A higher sedimentation rate results in lower retro-forearc subsidence of 1.85 km and lower extensional stress accumulation in the back-arc of 125 MPa compared to the 240 MPa in the model with lower erosion and sedimentation (Figures 9c and 9d).

Furthermore, we assessed these effects with two additional models (Figure S5 in Supporting Information S1) having an upper plate weak zone and a fixed lower plate during free-fall subduction. The trench retreat is solely accommodated by extension of the upper plate. These models show gradual forearc subsidence during slab steepening, and uplift during the rapid oceanic trench retreat and associated decreasing slab dip angle and during continental collision.

4. Discussion

4.1. Slab Dynamics Versus Stress Field and Surface Processes

The horizontally forced subduction initiation stage is associated with trench advance and upper plate compression. Contraction is partitioned between the forearc region leading to the development of a forearc high and a compressional retro-forearc depression. Furthermore, upper plate weak zones are partially reactivated and localize contraction in the back-arc region (Figures 4–6). This initial trench advance stage is associated with an increasing slab dip angle. Subsequent oceanic subduction is linked to slab roll-back and trench retreat. When slow convergence is assumed, such as observed in the Mediterranean (Le Pichon, 1982), upper plate compressional stress changes to the extension when the leading edge of the slab reaches ca. 300 km depth, and the onset of slab-rollback and trench retreat is modeled when the slab reaches ca. 380 km depth (Figure 4). Before the fast slab roll-back stage is reached monotonous slab steepening occurs (Figure 10). The slab dip angle decreases when the trench retreat velocity increases and after the slab reaches the model lower boundary. The maximum trench retreat velocity varies in the different models between 2.5 and 7.5 cm/yr (Figure 10) and it is accommodated by upper plate extension and back-arc crustal and lithospheric thinning. Following continental hard collision and the subduction of the buoyant continental crust, trench retreat switches to trench advance and results in upper plate compression prior to slab break-off.

In the models with different inherited weak zones, lithospheric thinning lasts for 10–25 Myr and the trench retreat velocity gradually increases until collision (Figure 5b) or until the slab reaches the bottom of the model (Figure 5d). Earlier trench retreat and faster slab roll-back is modeled when the upper plate is weaker, such as having both crustal and mantle weak zones or having higher thermal gradients (Hertgen et al., 2020; Figures S4 and S6 in Supporting Information S1). Steady roll-back is achieved after the slab is laid on top of the lower model boundary after the upper plate break-up (see videos in Supporting Information). Our 2D models imply that the trench retreat velocity is mainly controlled by the gradually increasing slab-pull force together with the increasing mantle return flow velocity that fosters slab roll-back, (e.g., Magni et al., 2012) and by the gradually decreasing strength of the upper plate during rifting (cf., Brune et al., 2016). Furthermore, notable trench retreat is only observed in the models where the upper plate is weakened, either above the simulated hydrated mantle wedge within the volcanic arc or due to inherited weak zones (Figure 10b). Previous studies inferred the role of viscous drag along the base of the upper plate that can contribute to back-arc extensional stresses, particularly for large

plates and higher asthenospheric viscosities (e.g., Capitanio et al., 2010). Our parameter test of different weak zone locations showed that earlier break-up and larger extension were modeled in case the zone was located at ca. 690 km from the accretionary wedge (Figure 6). This distance corresponds to the size of the poloidal mantle flow cell generated by the subducting slab (Figure 7) and shows the contribution of mantle flow to back-arc extension (cf., Yang et al., 2021; dal Zilio et al., 2018).

Stress transfer from the trench toward the upper plate is controlled by the strength and viscosity of the subduction interface (e.g., Billen & Gurnis, 2001; Buiter et al., 2001; Cerpa & Arcay, 2020; Cizkova & Bina, 2013). It has been demonstrated by similar thermo-mechanical models that realistic upper plate topography can be only achieved when a low viscosity mantle wedge is implemented (Billen & Gurnis, 2001). In our models, dehydration of the down-going slab leads to the development of a weak and hydrated mantle wedge (Figure 3; Faccenda et al., 2009).

The strength and effective viscosity of the subduction interface are also connected to the amounts of subducted weak sediments (Balázs, Faccenna, et al., 2021; Behr & Becker, 2018; Gerya & Stöckhert, 2002; Sobolev & Brown, 2019). Our models with different erosion and sedimentation rates (Table 2; Figures 8 and 9) show that the higher imposed sedimentation leads to a higher slab curvature radius and thus a shallower dipping slab, thicker sediment accumulation in the accretionary wedge, and more sediments are subducted deeper into the mantle (Figure 8). Furthermore, in our models, the higher sedimentation rate resulted in lower extensional stress accumulation in both the lower and upper continental plates, from 153 to 91 MPa and from 226 to 101 MPa, respectively, and lower horizontal compression (vertical tension) from 343 to 315 MPa within the lithospheric mantle underlying the forearc depocenter. Thicker sediments within the subduction interface also result in a wider zone of low viscosity subduction channel (4 vs. 3 km, where the viscosity is lower than 10^{21} Pa·s; Figure S7 in Supporting Information S1) and thus it creates less efficient stress transfer toward the upper plate that causes lower forearc subsidence values (Figure 8). Other models also showed that sediments or crustal slivers that accumulate beneath the forearc high contribute to its Myr-scale periodic vertical motions (Figure 7; Menant et al., 2020).

Previous studies suggested that lubrication of the subduction interface by sediments leads to increased subduction velocities during free-fall subduction (Behr & Becker, 2018; Sobolev & Brown, 2019). Our 2D simulations show the opposite effect, in agreement with the recent 3D simulations by Munch (2020) and 2D studies by Brizzi et al. (2021). Higher erosion and sedimentation rates lead to erosional unloading of the forearc high and contribute to additional sedimentary loading of the trench and lower plate. This material re-distribution leads to the following effects: (a) increased sediment subduction decreases the averaged density of the downgoing plate and decreases the slab pull force (cf., Brizzi et al., 2021), (b) the thicker and ca. 1.5 times wider accretionary wedge (cf. Figures 8a and 8b) increases the friction between the lower and upper plate and this leads to mechanical locking of the interface (Gerya & Stöckhert, 2002; Munch, 2020; Munch et al., 2019), and (c) material re-distribution modifies the slab curvature radius (Figure 8) and decreases the resistance of the slab against bending (cf., Buffett, 2006). The first two effects favor slower subduction, while the latter would cause subduction acceleration. Our models infer that the first two effects overcome the decreased slab bending resistance and therefore increased sedimentation leads to an overall lower subduction velocity compared with the models with a lower sedimentation rate. Maximum subduction velocities in the free-fall retreating models are 3.1 cm/yr versus 1.8 cm/yr, while in the models with a free lower plate the velocities are 7.1 cm/yr versus 4.8 cm/yr imposing lower and higher sedimentation, respectively (Figure 9). This is important for the topographic response because the higher subduction velocity leads to a higher negative dynamic topographic effect by ca. 2 km (Figure 9). These results need to be further studied by further 2D and 3D models incorporating elasto-visco-plastic rock rheologies and exploring a wider range of rheological properties, sediment densities, and other subducted rocks, which may alter the coupling and density structure of the forearc.

4.2. Modeled Forearc and Back-Arc Sedimentary Basin Evolution and Subsidence History

Two viable scenarios are proposed for forearc and back-arc basin evolution (Figure 1) depending on different rheological weakening mechanisms, such as melt induced weakening (Figure S1 in Supporting Information S1) and initial arc rifting shortly followed by oceanic spreading or strain localization at a larger distance from the arc along inherited zones within the overriding continent (Figure 4). The latter case is often connected to a long-lasting (ca. 12 Myr in our reference model, Figure 4) continental stretching phase prior to break-up (Figure 4). A short oceanic subduction stage only enables the development of an intra-continental extensional back-arc

basin (Figure 5). Forearc basin formation starts similarly in every model, connected to the development of the accretionary wedge and related wedge-top deformation and wedge-top forearc basin subsidence under variable compression and extensional pulses within the forearc region (Figures 4a–4c). Furthermore, accommodation space is created in the syncline structure of the retro-forearc basin. This means that forced subduction initiation leads to an early stage of retro-forearc basin subsidence prior to back-arc basin formation and subsidence.

Back-arc extension continues during the first million years of soft collision and continental subduction. During soft collision, that is, arrival of the extended passive margin into the subduction zone leads to rapid uplift of the trench and forearc regions (Figure 5a). This sudden uplift corresponds to the transition from deep marine *flysch* to continental *molasse* sedimentation as often interpreted in the Alpine-Mediterranean region (Figures 4f, 5a and 5b; Handy et al., 2015; Sinclair, 1997). Furthermore, the forearc region undergoes trench-ward tilting during fast trench retreat and rapid uplift when the slab reaches the bottom of the upper mantle (Figures 3 and 4). Finally, hard collision, that is, arrival of the thick continental lower plate leads to the cessation of back-arc extension and marks the onset of trench advance, orogenic build-up and back-arc basin inversion prior to slab break-off (Figure 3f).

4.3. Driving Forces of Forearc and Back-Arc Basin Subsidence and Uplift

Analysis of the upper plate stress field, slab dip, and trench retreat variations (Figure 10) contribute to understanding the main driving forces controlling forearc and back-arc basin subsidence (Figure 11). Subsidence of the retro-forearc basin is not isostatically compensated, as its 2–4 km tectonic subsidence occurs in the absence of notable crustal thickness variations. Our model results show that this region gradually subsides from the onset of forced subduction and the amount and rates of its subsidence are linked to the strength of the subduction interface, rheology of the upper plate, and the amount of subduction, slab dip angle, and slab bending in the mantle. The initial stage of retro-forearc subsidence of the wide (150–200 km) syncline structure is controlled by the initial trench advance and upper plate compressional flexure. The forearc crust and lithosphere show horizontal compressional stress fields (Figure 4a). It has been shown by previous similar studies that elasticity plays a major role in the distribution and magnitude of deviatoric stress and thus controls subduction dynamics and related topography (Bessat et al., 2020; Farrington et al., 2014; Fourel et al., 2014; Zhong & Gurnis, 1994). Elasticity contributes to a larger slab curvature radius and lower slab dip angle and thus it modifies the slab dynamics and upper plate deformation.

Following this early stage of compression-induced flexure, retro-forearc subsidence continues during the gradual slab steepening stage of subduction (Figure 10). Previous 3D models with laterally variable slab dip angles showed the lateral migration of fore-arc subsidence (Balazs et al., 2021a). The forearc crust and lithosphere show horizontal compression until 37.5 and 40 Myr in the reference model and in the strong homogenous model, respectively (Figures 4, 7 and 10). This subsidence by 37.5 Myr is ca. 250 m lower in the model, where the slab dip angle is lower, driven by the upper plate convergence (Figures 7 and 10). The locus of the retro-forearc depocenter overlies the deepest contact point of the subduction interface (Figure 4). This gradual subsidence is driven by the downward dragging of the slab connected to its increasing slab-pull force and the stress transfer through the subduction interface toward the base of the forearc lithosphere (Chen et al., 2017; Cerpa & Arcay, 2020; Hassani et al., 1997; Shemenda, 1993). This agrees with our results of models with different amounts of subducted sediments, where a thicker sediment accumulation in the interface lowers its strength and leads to lower stress accumulation in the upper plate that is associated with lower forearc subsidence (Figures 8 and 9). It has been also shown by previous models that this subsidence and the vertical stresses acting on the base of the upper plate are linked to the buoyancy of the slab (Crameri et al., 2017). Our models also show that gradual slab steepening contributes to forearc subsidence (cf., *Modhom* in Figure 6) due to the increasing buoyancy force of the deeper slab and increased stress transfer toward the upper plate over the interface. This means that the gradually steepening slab drags down the upper plate above the subduction interface (Cerpa & Arcay, 2020; Hassani et al., 1997; Shemenda, 1993). This explains why a steeper slab geometry results in larger forearc subsidence after the same amount of subduction (Figure 5).

An important stage of forearc evolution shows the gradual trench-ward tilting of the upper plate during subduction (Figures 4d and 7) that is associated with the subsidence of the former forearc high and corresponds to the slow uplift of the retro-forearc depocenter. During this stage, horizontal compressional stress decreases in the forearc crust, while vertical tensional stress increases at the base of the underlying mantle of the upper plate.

The main tensional stress axis is rotated toward the slab movement (Figure 11d). A similar tilting process is simulated by previous models during slab-transition-zone interaction, and it is proposed that upper plate tilting is caused by the larger-scale mantle flow pattern by excitation of the high-viscosity lower mantle (Crameri & Lithgow-Bertelloni, 2018). Analog models simulating solely the upper mantle reported a similar tilting event that is linked to variations in the vertical component of the trench suction along the interface during steady state slab roll-back (Chen et al., 2017). In our simulations upper plate trench-ward tilting commences before the leading edge of the slab reaches the bottom of the model, during the free-fall stage (Figures 4d and 7). This gradual tilting is observed from the onset of high-rate trench retreat and slab roll-back. During this phase, the slab dip angle decreases, the S-point retreats, and thus slab suction or drag will be more dominant in the shallower parts of the interface compared to the preceding slab steepening stage. In the model, where the upper plate is strong without any weak zones, the trench retreat and slab roll-back is suppressed compared with the reference model, and in this case, the forearc region records continuous subsidence until the slab reaches the bottom of the model (Figure 7). This implies that upper plate tilting is connected to slab unbending and related drag from the onset of the trench retreat and from the termination of slab steepening. Tilting may also be partly related to some internal rigidity of the rapidly retreating forearc, which experiences counter-clockwise rigid-body rotation when its leading-edge rides over less steep regions of the subducting plate. When the slab reaches the lower model boundary, that is, the base of the upper mantle, the vertical stresses at the base of the upper plate transmitted by the slab decrease. In the case of a high slab dip angle, for example, in the models with a strong and homogenous upper plate that prevents trench retreat, the slab shows an overturned geometry, and this is associated with the highest uplift rate (Figures 7a and 11h; Figure S8 in Supporting Information S1). In the case of lower slab dip angles, the slab lays on top of the transition zone which leads to slab unbending and further decreasing slab dip angle (Figures 5 and 7b). This is associated with decreasing forearc horizontal compression leading to the uplift of the previous forearc syncline and resulting in the trench-ward tilt of the upper plate (Figure 11).

Our results confirm that extensional back-arc basin subsidence is primarily controlled by crustal thinning driven by the retreating subduction trench relative to the upper plate (Figures 1 and 11). Slab roll-back, trench retreat, and extensional back-arc basin formation are connected to mantle flow and the buoyancy of the slab (Conrad & Hager, 1999; Faccenna et al., 2014; Magni et al., 2014; Wallace et al., 2009). When the convergence velocity remains low, subduction is partitioned into slab roll-back (Figure 10). Trench retreat and back-arc extension require a weak upper plate. Previous models either proposed high thermal gradients (Balázs, Faccenna, et al., 2021; Erdos et al., 2021; Gogus, 2015; Wolf & Huismans, 2019), assumed inherited crustal nappes or mantle weak suture zones (Balázs, Maţenco, et al., 2021; Menant et al., 2016; Yang et al., 2021) or rheological weakness created by the evolving hydrated mantle wedge and volcanic arc (Baitsch-Ghirardello et al., 2014; Magni, 2019). Back-arc rift localization is also supported by the underlying mantle convection cell (Figure 6; dal Zilio et al., 2018). In our upper mantle-scale model, the ca. 690 km distance from the trench favored the earliest back-arc rifting. During gradual roll-back and back-arc extension, the lithosphere of the upper plate gradually thins and thus its strength decreases contributing to speed up the back-arc extension (Figure 10).

A long wavelength (ca. 300–500 km) dynamic topographic signal is observed on the previous, shorter wavelength subsidence patterns. This dynamic topography is driven by vertical stresses imposed at the base of the upper plate driven by the underlying high velocity mantle flow (e.g., Faccenna & Becker, 2020; Husson, 2006). This effect is best illustrated in our free-fall subduction models (Figure 9). The gradually increasing mantle flow velocities from 1.5 to 7.1 cm/yr deflect the topography in the vicinity of the trench for both the lower and upper plates leading to additional subsidence of ca. 1.7 km. This corresponds to the deepening of the trench and trench-ward tilting of the upper plate (Figure 9). Therefore, our models simulate a shorter wavelength flexural, slab-induced dragging forearc subsidence and a mantle flow driven larger wavelength dynamic topographic signal.

4.4. Model Limitations and Outlook

Our high-resolution models only simulate the upper mantle. Complex slab – transition zone and lower mantle effects are not considered. Such an assumption is often used because of the significant viscosity increase in the lower mantle (e.g., Conrad & Hager, 1999) and the limited timescale of the modeled subduction history (Davies, 1995; Funiciello et al., 2003). Furthermore, in the case of the chosen Mediterranean subduction zones, seismic tomographic data infers that the Oligocene to Recent evolution of the region involved upper mantle subduction and convection history (cf., Wortel & Spakman, 2000). In our 2D setup, 3D mantle flow effects

cannot be simulated, although it has been shown that toroidal mantle flow plays a major role in back-arc extension, while our models overestimate the poloidal mantle flow component. Our regional-scale model domain only allowed the simulation of one slab, while global 3D subduction models (e.g., Coltice et al., 2019; Tackley, 2000) also address more complex slab and mantle flow interactions. The simulations including melt extraction only handled visco-plastic rheologies. Finally, we have not focused on the role of mantle delamination, slab break-off or slab tear propagation. Previous 2D and 3D models (Duretz et al., 2011, 2014) show that such events can also produce rapid uplift rates in the order of 0.2–0.5 km/Myr depending on the depth of deformation and plate rheology.

4.5. Comparison With Mediterranean Subduction Zones

We compare our model results with the evolution of forearc and back-arc basins formed on the overriding plates of Mediterranean subduction zones.

4.5.1. Evolution of the Pannonian-Transylvanian-Carpathians System

The Pannonian-Transylvanian Basin is surrounded by the Alpine-Carpathians-Dinarides orogens in Central Europe (Figure 2). The Pannonian Basin is floored by 22–25 km thinned continental crust including on average 2–4 km thick Miocene to Recent sediments (Kalmár et al., 2021). The basin overlies an attenuated lithosphere of ca. 50–60 km resulting in 100–120 mW/m^2 high surface heat flow (Horváth et al., 2015; Lenkey et al., 2002; Tari et al., 1999). In contrast, the Transylvanian Basin has ca. 35 km thick crust and it has a lower surface heat flow of 45 mW/m^2, only the closest vicinity of volcanic edifices shows high 110 mW/m^2 values (Tilita et al., 2013).

The formation of the Pannonian and Transylvanian Basins followed the Mesozoic opening and subsequent closure of two oceanic realms connected to the evolution of the larger Neotethys and the Alpine Tethys oceans. The Neotethyan branch opened during the Middle Triassic and was closed by late Jurassic-Cretaceous subduction and collision resulting in a suture in the transition between the present-day Pannonian Basin and Dinarides, creating the Sava suture zone. The area presently enclosed by the Carpathians was occupied by the land-locked partly oceanic and partly continental hyperextended basin, that formed during the Jurassic related to the Alpine Tethys spreading, and its subduction was initiated in the Late Cretaceous. The upper plate of the Carpathian embayment subduction was composed of two megaunits with different paleogeographic origins. The AlCaPa megaunit in the north derived from the Alpine orogenic wedge, while Tisza-Dacia in the South detached from the Dinaridic margin (Figure 2b; Csontos & Vörös, 2004; van Hinsbergen et al., 2020; Horváth et al., 2015; Matenco & Radivojević, 2012). This pre-rift orogenic evolution resulted in similar crustal or mantle inherited weak zones as the implemented ones in our and similar numerical models (Balázs, Maţenco, et al., 2021; Fodor et al., 2021).

The recent, narrow remnant of the slab connected to the formation and evolution of the Pannonian-Transylvanian basins is presently imaged beneath the SE Carpathians (Wortel & Spakman, 2000) and it is in the process of break-off (Ismail-Zadeh et al., 2012). Eastward, ca. 200–300 km slab rollback accommodated the continental extension of the Pannonian back-arc basin. The age of the oldest syn-rift sediments, exhumation ages of metamorphic cores, and ages of calc-alkaline volcanism point to a ca. 20–22 Ma onset of extension that was first localized along the inherited Sava suture zone along the Dinaridic margin. Deformation gradually migrated toward the center of the basin until ca. 9 Ma (Balázs, Maţenco, et al., 2021; Horváth et al., 2015; Lukács et al., 2018; Matenco & Radivojević, 2012; Ustaszewski et al., 2010).

Different evolutionary models have been proposed to explain the subsidence of the Transylvanian Basin. Crustal down-warping due to the pull of the retreating slab was proposed by Royden et al. (1982) to explain the Miocene basin subsidence. Krézsek and Bally (2006) proposed a multi-stage evolution, including Upper Cretaceous rifting and subsequent inversion and Paleogene sagging, followed by Lower Miocene flexural basin development and gravitational spreading. Later studies (Matenco & Radivojević, 2012; Tilita et al., 2013) emphasized the connection between the evolution of the Pannonian and Transylvanian Basins by lithospheric-scale simple shear mechanism and lower crustal flow effects. The late Miocene to the recent uplift of the Transylvanian Basin is interpreted to be the effect of the ongoing slab detachment beneath the SE Carpathians (Wortel & Spakman, 2000) coupled with mantle delamination (Gogus & Ueda, 2018) and further mantle flow effects (Sengul-Uluocak et al., 2019) and related volcanism (Gartner et al., 2020).

Our model results with a smaller oceanic basin can be compared with the crustal and lithospheric thinning and extensional back-arc subsidence of the Pannonian Basin and the notably non-extensional subsidence and late-stage uplift of the Transylvanian Basin. The onset of compression induced subsidence in the forearc is coeval with back-arc contraction and uplift caused by forced subduction initiation (Figure 5). During free-fall subduction, the inherited weak zone localized extensional deformation resulting in crustal and mantle thinning and back-arc basin subsidence, while continuous sag subsidence took place in the forearc basin driven by slab steepening and downward dragging. Continental subduction marked the uplift of the forearc basin, while back-arc extension continued until the hard collision. This collision leads to the structural inversion of the extensional back-arc basin superimposed on its thermal cooling (Bada et al., 2007; Fodor et al., 2021, Figures 2b, 5b and 11). The model with the converging upper plate (Modtwfr in Table 2; Figure S5 in Supporting Information S1) enables the most suitable comparison with the kinematics of the Carpathian subduction zone. During free-fall subduction and negligible convergence, slab roll-back is purely accommodated by upper plate extension creating a continental extensional basin, while forearc subsidence is driven by the dragging of the slab. Finally, after the slab roll-back velocity ceases, the back-arc basin still subsides driven by thermal cooling, while the forearc basin records uplift due to the ongoing mantle convection and by the onset of slab necking prior to break-off.

4.5.2. Evolution of the Calabrian-Tyrrhenian System

The Tyrrhenian back-arc, Paola forearc basins, and the Calabrian accretionary wedge in the central Mediterranean formed during the Neogene subduction and trench roll-back of the Ionian oceanic slab (Figure 2c). Seismic tomography and previous reconstructions infer ca. 1,000 km subduction and 800 km trench retreat beside the additional 200 km plate convergence in the case of the southern Tyrrhenian since 30 Ma (e.g., Faccenna et al., 2014). The relict of the originally larger subduction zone is imaged today as a narrow, deep, and steep NW dipping slab (Faccenna et al., 2014 and references therein). Trench retreat was accommodated by upper plate extension and crustal thinning of the Tyrrhenian Basin leading to the overall eastward migration of deformation (e.g., Loreto et al., 2021; Minelli & Faccenna, 2010; Rosenbaum & Lister, 2004).

The crust gradually thins from 40 km in Calabria to 30 km below the Paola Basin, the latter hosts ca. 4.5 km thick Plio-Quaternary sediments in an overall syncline geometry (Corradino et al., 2020). Further west toward the Tyrrhenian Sea crustal thickness gradually decreases and is entirely attenuated in the Vavilov and Marsili Basins leading to mantle exhumation and localized spreading (Figure 2c; Nicolosi et al., 2006). Surface heat flow is ca. 50–80 mW/m^2 in the Paola Basin, while in the Tyrrhenian Basin this value reaches 150–250 mW/m^2 due to the attenuated lithosphere (Zito et al., 2003).

The evolution of the Tyrrhenian can be compared with our model with the longer oceanic lower plate, where the larger trench retreat values resulted in back-arc crustal break-up (Figures 4 and 11). Similar to the model results, trench retreat shows an initial slow velocity for the first 10 Myr of subduction. Slab roll-back and trench retreat speed up between 6 and 3 Ma and slow down again from 3 Ma to the present (Minelli & Faccenna, 2010). The highest trench retreat velocity is inferred during the opening of the Vavilov and Marsili Basins, reaching higher values between 2.1 and 1.6 Myr (Nicolosi et al., 2006). Similar dynamics are observed in our models (Figures 4 and 10; Figure S1 in Supporting Information S1), where the initial gradual increase of slab roll-back velocity is controlled by the gradually increasing slab-pull force and mantle return flow, while the subsequent velocity decrease is simulated after the slab reaches the bottom of the upper mantle and following continental subduction (Figures 4 and 10). Furthermore, the highest roll-back velocities are observed during the last stages of back-arc rifting and during back-arc spreading when the upper plate strength and related resistance mitigate (Figures 5c and 10). In agreement with our models (Figures 4 and 5), extensional deformation was initially distributed over a larger area, initially located at a larger distance from the subduction zone, and subsequently migrated toward the volcanic arc (e.g., Loreto et al., 2021; Rosenbaum & Lister, 2004). While subsidence of the Tyrrhenian Basin was controlled by extension and crustal thinning, subsidence of the Paola Basin is not accommodated by major normal faults (Pepe et al., 2010). Its syncline geometry and its position between the Aeolian Volcanic arc and the accretionary wedge infers its tectonic origin as a similar retro-forearc basin as in our models (Figure 2; Corradino et al., 2020) controlled by moderate contraction and slab dragging being coeval with the extension of the Tyrrhenian back-arc basin. This evolution was overprinted by the trench-ward migration of the volcanic arc and related arc rifting (Figure S1 in Supporting Information S1; Corradino et al., 2020).

4.5.3. Evolution of the Alboran System

Evolution of the western Mediterranean region is confined between the larger African and Eurasian plates and the Iberian plate (Jimenez-Munt et al., 2019). Surrounded by these plates, subduction of an oceanic segment of the Alpine Tethys slab resulted in the formation of the West Alboran forearc basin and the East Alboran and Algerian extensional back-arc basins (Do Couto et al., 2016). The remnant of this slab is imaged today beneath the West Alboran Sea and southern Spain (Figure 2). The 3D complexity of this region led to still debated tectonic reconstructions (e.g., Faccenna et al., 2014; Spakman & Wortel, 2004; Vergés & Fernàndez, 2012). Our simplified 2D models do not aim to decipher the complex 3D paleogeographic history of the Alboran domain but contribute to understanding the subsidence and uplift patterns of the forearc and back-arc basins of this subduction zone.

The highest crustal thickness in the region is measured beneath the Gibraltar arc and reaches ca. 45 km. An imbricated sedimentary wedge is formed in the Gulf of Cadiz overlying the Atlantic oceanic domain. The crustal thickness gradually decreases eastwards having 30–40 km beneath the West Alboran Basin and evolves into a thinned continental and oceanic crust toward the East Alboran and Algerian Basin, respectively (Figure 2; Comas et al., 1999; Villasenor et al., 2015). The West Alboran Basin has a lower thermal gradient and a lower surface heat flow of ca. 40–80 mW/m^2, while this is up to 130 mW/m^2 in the eastern Alboran Basin reflecting the gradual lithospheric thinning toward the most extended back-arc domain (Torne et al., 2000).

Similar to the above mentioned Transylvanian and Paola basins, the evolution of the West Alboran Basin has been debated and has been considered either as a back-arc or forearc basin (d'Acremont et al., 2020; Do Couto et al., 2016). Our model results are in agreement with high resolution seismic interpretation (Figure 2d) inferring the forearc nature of the West Alboran Basin implying slab suction and compression as the main basin forming mechanisms, while back-arc extensional deformation was localized at larger distances within the East Alboran and Algerian basins.

5. Conclusions

Subsidence and uplift rates of forearc and back-arc basins are controlled by variations in plate convergence and subduction velocities and governed by different plate rheologies and surface processes. Our model results led to the following main conclusions.

Accommodation space and sedimentary basins are formed on top of the accretionary wedge creating piggy-back or wedge-top forearc basins, while retro-forearc basins are formed on the overriding continental plate in a wide syncline structure overlying the subduction interface at ca. 200 km distance from the accretionary wedge between a forearc high and the volcanic arc.

Horizontally forced subduction initiation leads to an early stage of compression-induced forearc subsidence. Its syn-kinematic stratigraphic age can constrain the age of subduction initiation. Back-arc basin formation and subsidence begin 25–35 Myr later, governed by the increasing slab pull force, mantle flow, and the strength of the upper plate. Slab steepening leads to forearc subsidence, while a decreasing slab dip and slab unbending results in forearc uplift and upper plate trench-ward tilting. Soft collision and slab transition zone interaction contribute to forearc uplift, while back-arc subsidence continues until the hard collision.

The retro-forearc subsidence is amplified by gradually increasing slab-pull force acting on the slab and by the slab-induced dragging, imposing tensional stresses at the base of the upper plate. A weaker subduction interface, for example, by enhanced sediment subduction enables less efficient stress transfer and leads to lower forearc subsidence. During free-fall subduction and the climax of slab roll-back the forearc high subsides beneath sea level and the locus of the forearc depocenter migrates trench-ward reflected by upper plate tilting. Models simulating free-fall subduction without any imposed velocity constraint led to high subduction and mantle flow velocities up to 7 cm/yr and result in the highest negative dynamic topographic signal within the trench and in the upper plate. Ultimately, continental subduction or after the slab reaches the bottom of the upper mantle, the forearc basin records rapid uplift.

The back-arc region of the upper plate records compression or extension based on the dynamics of subduction and convergence velocities. Back-arc subsidence is mainly controlled by crustal thinning governed by slab roll-back. Back-arc deformation localizes in the upper plate along inherited crustal or mantles weak zones often hundreds

of kilometers from the trench. Back-arc extension velocity gradually increases by the increasing slab pull and increasing mantle return flow effect, further facilitated by the gradually decreasing strength of the progressively thinned overriding plate. Back-arc spreading marks a sudden acceleration of back-arc extension.

Our modeling results detail the evolution of subduction zones with similar settings and characteristics as Mediterranean subduction zones and the comparison suggests that Western-Eastern Alboran, Paola-Tyrrhenian, Transylvanian-Pannonian Basins should be considered as genetically connected forearc – back-arc basins, respectively.

Data Availability Statement

The numerical code presented in this study is available online (https://doi.org/10.5281/zenodo.6320858).

Acknowledgments
All numerical models were run on the Euler and Leonhard clusters at ETH Zurich. AB acknowledges financial support from the ETH Zurich Postdoctoral Fellowship program. TG and AB acknowledge SNSF grant 192296. The Grant to Department of Science, Roma Tre University (Miur-Italy Dipartimenti di Eccellenza, Commi 314–337 Legge 232/2016) is acknowledged by CF and FF. Luca Dal Zilio is acknowledged for his help with data visualization. We acknowledge two anonymous reviewers and the Associate Editor Laurent Husson for their constructive and detailed comments. Open access funding provided by Eidgenossische Technische Hochschule Zurich.

References

Bada, G., Horváth, F., Dövényi, P., Szafián, P., Windhoffer, G., & Cloetingh, S. (2007). Present-day stress field and tectonic inversion in the Pannonian basin. *Global and Planetary Change*, *58*(1–4), 165–180.

Baitsch-Ghirardello, B., Gerya, T. V., & Burg, J.-P. (2014). Geodynamic regimes of intra-oceanic subduction: Implications for arc extension vs. shortening processes. *Gondwana Research*, *25*, 546–560.

Balázs, A., Faccenna, C., Ueda, K., Funiciello, F., Boutoux, A., Blanc, E. J.-P., & Gerya, T. (2021). Oblique subduction and mantle flow control on upper plate deformation: 3D geodynamic modeling. *Earth and Planetary Science Letters*, *569*. https://doi.org/10.1016/j.epsl.2021.117056

Balázs, A., Maţenco, L., Granjeon, D., Vogt, K., Francois, T., & Sztanó, O. (2021). Towards stratigraphic thermo-mechanical numerical modelling: Integrated analysis of asymmetric extensional basins. *Global and Planetary Changes*, *196*. https://doi.org/10.1016/j.gloplacha.2020.103386

Balázs, A., Matenco, L., Vogt, K., Cloetingh, S., & Gerya, T. (2018). Extensional polarity change in continental rifts: Inferences from 3-D numerical modeling and observations. *Journal of Geophysical Research: Solid Earth*, *123*, 8073–8094. https://doi.org/10.1029/2018JB015643

Behr, W. M., & Becker, T. W. (2018). Sediment control on subduction plate speeds. *Earth and Planetary Science Letters*, *502*, 166–173. https://doi.org/10.1016/j.epsl.2018.08.057

Bessat, A., Duretz, T., Hetenyi, G., Pilet, S., & Schmalholz, S. M. (2020). Stress and deformation mechanisms at a subduction zone: Insights from 2-D thermomechanical numerical modelling. *Geophysical Journal International*, *221*, 1605–1625. https://doi.org/10.1093/gji/ggaa092

Billen, M. I., & Gurnis, M. (2001). A low viscosity wedge in subduction zones. *Earth and Planetary Science Letters*, *193*, 227–236.

Braun, J. (2010). The many surface expressions of mantle dynamics. *Nature Geoscience*, *3*, 825–833.

Brizzi, S., Becker, T. W., Faccenna, C., Behr, W., vanZelst, I., Dal Zilio, L., & vanDinther, Y. (2021). Control of sediments on subduction dynamics and geometry. *Geophysical Research Letters*, *48*, e2021GL096266.

Brun, J.-P., & Faccenna, C. (2008). Exhumation of high-pressure rocks driven by slab rollback. *Earth and Planetary Science Letters*, *272*, 1–7.

Brun, J. P., & Sokoutis, D. (2010). 45 m.y. of Aegean crust and mantle flow driven by trench retreat. *Geology*, *38*(9), 815–818. https://doi.org/10.1130/G30950.1

Brune, S., Williams, S. E., Butterworth, N. P., & Müller, R. D. (2016). Abrupt plate accelerations shape rifted continental margins. *Nature*, *536*, 201–204.

Buffett, B. A. (2006). Plate force due to bending at subduction zones. *Journal of Geophysical Research*, *111*, B09405. https://doi.org/10.1029/2006JB004295

Buiter, S. J. H., Govers, R., & Wortel, M. J. R. (2001). A modeling study of vertical surface displacements at convergent plate margins. *Geophysical Journal International*, *147*, 415–427. https://doi.org/10.1046/j.1365-246X.2001.00545.x

Burov, E. (2011). Rheology and strength of the lithosphere. *Marine and Petroleum Geology*, *28*, 1402–1443.

Capitanio, F. A., Stegman, D. R., Moresi, L. N., & Sharples, W. (2010). Upper plate controls on deep subduction, trench migrations and deformations at convergent margins. *Tectonophysics*, *483*, 80–92.

Cerpa, N. G., & Arcay, D. (2020). Overriding plate velocity control on surface topography in 2-D models of subduction zones. *Geochemistry, Geophysics, Geosystems*, *21*, e2019GC008900.

Chen, Z., Schellart, W., & Duarte, J. (2015). Overriding plate deformation and variability of fore-arc deformation during subduction: Insight from geodynamic models and application to the Calabria subduction zone. *Geochemistry, Geophysics, Geosystems*, *16*, 3697–3715. https://doi.org/10.1002/2015GC005958

Chen, Z., Schellart, W., Duarte, J., & Strak, V. (2017). Topography of the overriding plate during progressive subduction: A dynamic model to explain forearc subsidence. *Geophysical Research Letters*, *44*, 9632–9643.

Cizkova, H., & Bina, C. R. (2013). Effects of mantle and subduction-interface rheologies on slab stagnation and trench rollback. *Earth and Planetary Science Letters*, *379*, 95–103.

Coltice, N., Laurent, H., Faccenna, C., & Maëlis, A. (2019). What drives tectonic plates? *Science Advances*, *5*, 4295. https://doi.org/10.1126/sciadv.aax4295

Comas, M. C., Platt, J. I., Soto, J. J., & Watts, A. B. (1999). The origin and tectonic history of the Alboran Basin: Insights from Leg 161 results. *The Proceedings of the Ocean Drilling Program*, *161*, 555–579.

Connolly, J. A. D. (2005). Computation of phase equilibria by linear programming: A tool for geodynamic modeling and its application to subduction zone decarbonation. *Earth and Planetary Science Letters*, *236*, 524–541.

Conrad, C. P., & Hager, B. H. (1999). Effects of plate bending and fault strength at subduction zones on plate dynamics. *Journal of Geophysical Research*, *104*, 60717551–60717571.

Corradino, M., Pepe, F., Bertotti, G., Picotti, V., Monaco, C., & Nicolich, R. (2020). 3-D architecture and Plio-Quaternary evolution of the Paola basin: Insights into the forearc of the Tyrrhenian-Ionian subduction system. *Tectonics*, *39*, e2019TC005898. https://doi.org/10.1029/2019TC005898

Crameri, F., & Lithgow-Bertelloni, C. (2018). Abrupt upper-plate tilting during slab-transition-zone collision. *Tectonophysics*, *746*, 199–211.

Crameri, F., Lithgow-Bertelloni, C. R., & Tackley, P. J. (2017). The dynamical control of subduction parameters on surface topography. *Geochemistry, Geophysics, Geosystems*, *18*, 1661–1687.

Crameri, F., Schmeling, H., Golabek, G. J., Duretz, T., Orendt, R., Buiter, S. J. H., et al. (2012). A comparison of numerical surface topography calculations in geodynamic modelling: An evaluation of the 'sticky air' method. *Geophysical Journal International*, *189*(1), 38–54. https://doi.org/10.1111/j.1365-246X.2012.05388.x

Csontos, L., & Vörös, A. (2004). Mesozoic plate tectonic reconstruction of the Carpathian region. *Palaeogeography, Palaeoclimatology, Palaeoecology*, *210*(1), 1–56. https://doi.org/10.1016/j.palaeo.2004.02.033

d'Acremont, E., Lafosse, M., Rabaute, A., Teurquety, G., Do Couto, D., Ercilla, G., et al. (2020). Polyphase tectonic evolution of fore-arc basin related to STEP fault as revealed by seismic reflection data from the Alboran Sea (W-Mediterranean). *Tectonics*, *39*, e2019TC005885. https://doi.org/10.1029/2019TC005885

Dal Zilio, L., Faccenda, M., & Capitanio, F. (2018). The role of deep subduction in supercontinent breakup. *Tectonophysics*, *746*, 312–324.

Davies, G. F. (1981). Regional compensation of subducted lithosphere: Effects on geoid, gravity and topography from a preliminary model. *Earth and Planetary Science Letters*, *54*, 431–441.

Davies, G. F. (1995). Penetration of plates and plumes through the mantle transition zone. *Earth Planetary and Science Letters*, *133*, 507–516.

Dewey, J. F., Helman, M. L., Turco, E., Hutton, D. H. W., & Knott, S. D. (1989). Kinematics of the Western Mediterranean. In M. P. Coward, D. Dietrich, & R. G. Park (Eds.), *Alpine Tectonics*. *Geological Society Special Publications* (Vol. 45, pp. 265–283). Geological Society of London.

Diaferia, G., Cammarano, F., & Faccenna, C. (2019). Thermal structure of a vanishing subduction system: An example of seismically-derived crustal temperature along the Italian peninsula. *Geophysical Journal International*, *219*, 239–247.

Dickinson, W. R., & Seely, D. R. (1979). Structure and stratigraphy of forearc regions. *AAPG Bulletin*, *63*(1), 2–31.

Do Couto, D., Gorini, C., Jolivet, L., Lebret, N., Augier, R., Gumiaux, C., et al. (2016). Tectonic and stratigraphic evolution of the Western Alboran Sea basin in the last 25 Myrs. *Tectonophysics*, *677*(678), 280–311. https://doi.org/10.1016/j.tecto.2016.03.020

Duretz, T., Gerya, T. V., & May, D. (2011). Numerical modelling of spontaneous slab breakoff and subsequent topographic response. *Tectonophysics*, *502*, 244–256.

Duretz, T., Gerya, T. V., & Spakman, W. (2014). Slab detachment in laterally varying subduction zones: 3-D numerical modeling. *Geophysical Research Letters*, *41*, 1951–1956. https://doi.org/10.1002/2014GL059472

Dymkova, D., Gerya, T., & Burg, J.-P. (2016). 2D thermomechanical modelling of continent–arc–continent collision. *Gondwana Research*, *32*, 138–150.

Erdos, Z., Huismans, R., Faccenna, C., & Wolf, S. G. (2021). The role of subduction interface and upper plate strength on Back-arc extension: Application to Mediterranean Back-arc basins. *Tectonics*, *40*(8), e2021TC006795. https://doi.org/10.1029/2021TC006795

Espurt, N., Funiciello, F., Martinod, J., Guillaume, B., Regard, V., Faccenna, C., & Brusset, S. (2008). Flat subduction dynamics and deformation of the south American plate: Insights from analog modeling. *Tectonics*, *27*, TC3011. https://doi.org/10.1029/2007TC002175

Faccenda, M., Gerya, T. V., & Burlini, L. (2009). Deep slab hydration induced by bending-related variations in tectonic pressure. *Nature Geoscience*, *2*, 790–793.

Faccenna, C., & Becker, T. (2020). Topographic expressions of mantle dynamics in the Mediterranean. *Earth-Science Reviews*, *209*, 103327.

Faccenna, C., Becker, T. W., Auer, L., Billi, A., Boschi, L., Brun, J. P., et al. (2014). Mantle dynamics in the Mediterranean. *Reviews on Geophysics*, *52*, 283–332. https://doi.org/10.1002/2013RG000444

Farrington, R. J., Moresi, L.-N., & Capitanio, F. A. (2014). The role of viscoelasticity in subducting plates. *Geochemistry, Geophysics, Geosystems*, *15*, 4291–4304. https://doi.org/10.1002/2014GC005507

Flament, N., Gurnis, M., & Muller, R. D. (2013). A review of observations and models of dynamic topography. *Lithosphere*, *5*(2), 189–210.

Fodor, L., Balázs, A., Csillag, G., Dunkl, I., Heja, G., Jelen, B., et al. (2021). Crustal exhumation and depocenter migration from the Alpine orogenic margin towards the Pannonian extensional back-arc basin controlled by inheritance. *Global and Planetary Change*, *201*, 103475. https://doi.org/10.1016/j.gloplacha.2021.103475

Forsyth, D. W., & Uyeda, S. (1975). On the relative importance of the driving forces of plate motion. *Geophysical Journal International*, *43*, 163–200.

Fourel, L., Goes, S., & Morra, G. (2014). The role of elasticity in slab bending. *Geochemistry, Geophysics, Geosystems*, *15*, 4507–4525.

Fuller, C. W., Willett, S. D., & Brandon, M. T. (2006). Formation of forearc basins and their influence on subduction zone earthquakes. *Geology*, *34*, 65–68.

Funiciello, F., Faccenna, C., Giardini, D., & Regenauer-Lieb, K. (2003). Dynamics of re-treating slabs: 2. Insights from three-dimensional laboratory experiments. *Journal of Geophysical Research*, *108*(B4), 2207. https://doi.org/10.1029/2001JB000896

Gartner, B. A. J. J., Seghedi, I., Nikogosian, I. K., & Mason, P. R. D. (2020). Asthenosphere-induced melting of diverse source regions for East Carpathian post-collisional volcanism. *Contributions to Mineralogy and Petrology*, *175*, 54. https://doi.org/10.1007/s00410-020-01690-4

Gerya, T. V. (2010). *Introduction to numerical geodynamic modelling* (p. 345). Cambridge University Press.

Gerya, T. V., & Meilick, F. I. (2011). Geodynamic regimes of subduction under an active margin: Effects of rheological weakening by fluids and melts. *Journal of Metamorphic Geology*, *29*, 7–31.

Gerya, T. V., & Stöckhert, B. (2002). Exhumation rates of high pressure metamorphic rocks in subduction channels: The effect of Rheology. *Geophysical Research Letters*, *29*, 1021–1024.

Gerya, T. V., & Yuen, D. A. (2007). Robust characteristics method for modelling multiphase visco-elasto-plastic thermo-mechanical problems. *Physics of the Earth and Planetary Interiors*, *163*, 83–105.

Göğüş, O. H. (2015). Rifting and Subsidence following lithospheric removal in continental back-arcs. *Geology*, *43*, 3–6. https://doi.org/10.1130/G36305.1

Gogus, O. H., & Ueda, K. (2018). Peeling back the lithosphere: Controlling parameters, surface expressions and the future directions in delamination modeling. *Journal of Geodynamics*, *117*, 21–40.

Gorczyk, W., Willner, A. P., Gerya, T. V., Connolly, J. A. D., & Burg, J.-P. (2007). Physical controls of magmatic productivity at Pacific-type convergent margins: Numerical modelling. *Physics of the Earth and Planetary Interiors*, *163*, 209–232.

Handy, M. R., Ustaszewski, K., & Kissling, E. (2015). Reconstructing the Alps–Carpathians–Dinarides as a key to understanding switches in subduction polarity, slab gaps and surface motion. *International Journal of Earth Sciences*, *104*, 1–26.

Hassani, R., Jongmans, D., & Chery, J. (1997). Study of plate deformation and stress in subduction processes using two-dimensional numerical models. *Journal of Geophysical Research*, *102*, 17951–17965.

Hertgen, S., Yamato, P., Guillaume, B., Magni, V., Schliffke, N., & vanHunen, J. (2020). Influence of the thickness of the overriding plate on convergence zone dynamics. *Geochemistry, Geophysics, Geosystems*, *21*, e2019GC008678.

Holmes, A. (1944). *Principles of physical Geology. 189–190*. Thomas Nelson and Sons.

Horváth, F., Musitz, B., Balázs, A., Végh, A., Uhrin, A., Nádor, A., et al. (2015). Evolution of the Pannonian basin and its geothermal resources. *Geothermics*, *53*, 328–352.

Husson, L. (2006). Dynamic topography above retreating subduction zones. *Geology*, *34*, 741–744.
Husson, L., Guillaume, B., Funiciello, F., Faccenna, C., & Royden, L. H. (2012). Unraveling topography around subduction zones from laboratory models. *Tectonophysics*, *526–529*, 5–15. https://doi.org/10.1016/j.tecto.2011.09.001
Ismail-Zadeh, A., Matenco, L., Radulian, M., Cloetingh, S., & Panza, G. (2012). Geodynamics and intermediate-depth seismicity in Vrancea (the south-eastern Carpathians): Current state-of-the art. *Tectonophysics*, *530*, 50–79.
Jiménez-Munt, I., Torne, M., Fernàndez, M., Vergés, J., Kumar, A., Carballo, A., et al. (2019). Deep seated density anomalies across the Iberia-Africa plate boundary and its Origin and development of marginal basins in the Western Pacific. *Journal of Geophysical Research*, *76*(11), 2542–2561.
Jolivet, L., Faccenna, C., & Piromallo, C. (2009). From mantle to crust: Stretching the Mediterranean. *Earth and Planetary Science Letters*, *285*, 198–209.
Jolivet, L., Menant, A., Clerc, C., Sternai, P., Bellahsen, N., Leroy, S., et al. (2018). Extensional crustal tectonics and crust-mantle coupling, a view from the geological record. *Earth-Science Reviews*, *185*, 1187–1209.
Kalmár, D., Hetényi, G., Balázs, A., Bondár, I., & AlpArray Working Group. (2021). Crustal thinning from orogen to back-arc basin: The structure of the Pannonian Basin region revealed by P-to-S converted seismic waves. *Journal of Geophysical Research: Solid Earth*, *126*, e2020JB021309. https://doi.org/10.1029/2020JB021309
Karig, D. E. (1971). Origin and development of marginal basins in the western Pacific. *Journal of Geophysical Research*, *76*(11), 2542–2561.
Krézsek, C., & Bally, A. W. (2006). The Transylvanian Basin (Romania) and its relation to the Carpathian fold and thrust belt: Insights in gravitational salt tectonics. *Marine and Petroleum Geology*, *23*, 405–442.
Le Breton, E., Brune, S., Ustaszewski, K., Zahirovic, S., Seton, M., & Müller, R. D. (2021). Kinematics and extent of the piemont–liguria basin—implications for subduction processes in the Alps. *Solid Earth*, *12*(4), 885–913. https://doi.org/10.5194/se-12-885-2021
Lenkey, L., Dovenyi, P., Horvath, F., & Cloetingh, S. A. P. L. (2002). Geothermics of the Pannonian Basin and its bearing on neotectonic. In S. Cloetingh, F. Horvath, G. Bada, & A. Lankreijer (Eds.), *Neotectonics and surface processes: The Pannonian Basin and Alpine/Carpathians system*, *European Geosciences Union* (Vol. 3, pp. 29–40). Stephan Mueller Special Publications.
Le Pichon, X. (1982). *Land-locked ocean basin and continental collision in the eastern Mediterranean area as a case example: Mountain building processes* (pp. 201–213). Academic Press.
Li, Z. H., Xu, Z., Gerya, T., & Burg, J. P. (2013). Collision of continental corner from 3-d numerical modeling. *Earth and Planetary Science Letters*, *380*, 98–111. https://doi.org/10.1016/j.epsl.2013.08.034
Loreto, M. F., Zitellini, N., Ranero, C. R., Palmiotto, C., & Prada, M. (2021). Extensional tectonics during the Tyrrhenian back-arc basin formation and a new morphotectonic map. *Basin Research*. https://doi.org/10.1111/bre.12458
Lukács, R., Harangi, S., Guillong, M., Bachmann, O., Fodor, L., Buret, Y., et al. (2018). Early to Mid-Miocene syn-extensional massive silicic volcanism in the Pannonian Basin (East-Central Europe): Eruption chronology, correlation potential and geodynamic implications. *Earth-Science Reviews*, *179*, 1–19. https://doi.org/10.1016/j.earscirev.2018.02.005
Magni, V. (2019). The effects of back-arc spreading on arc magmatism. *Earth and Planetary Science Letters*, *519*, 141–151.
Magni, V., Faccenna, C., van Hunen, J., & Funiciello, F. (2014). How collision triggers backarc extension: Insight into Mediterranean style of extension from 3-D numerical models. *Geology*, *42*, 511–514.
Magni, V., van Hunen, J., Funiciello, F., & Faccenna, C. (2012). Numerical models of slab migration in continental collision zones. *Solid Earth*, *3*, 293–306.
Mannu, U., Ueda, K., Willett, S. D., Gerya, T. V., & Strasser, M. (2017). Stratigraphic signatures of forearc basin formation mechanisms. *Geochemistry, Geophysics, Geosystems*, *18*, 2388–2410. https://doi.org/10.1002/2017GC006810
Matenco, L., & Radivojević, D. (2012). On the formation and evolution of the Pannonian Basin: Constraints derived from the structure of the junction area between the Carpathians and Dinarides. *Tectonics*, *31*, TC6007. https://doi.org/10.1029/2012TC003206
Medialdea, T., Vegas, R., Somoza, L., Vazquez, J. T., Maldonado, A., Díaz-del-Río, V., et al. (2004). Structure and evolution of the "Olistostrome" complex of the Gibraltar arc in the Gulf of Cadiz (eastern central Atlantic): Evidence from two long seismic cross-sections. *Marine Geology*, *209*, 173–198.
Menant, A., Angiboust, S., Gerya, T., Lacassin, R., Simoes, M., & Grandin, R. (2020). Transient stripping of subducting slabs controls periodic forearc uplift. *Nature Communications*, *11*, 1823. https://doi.org/10.1038/s41467-020-15580-7
Menant, A., Sternai, P., Jolivet, L., Guillou-Frottier, L., & Gerya, T. (2016). 3D numerical modeling of mantle flow, crustal dynamics and magma Genesis associated with slab roll-back and tearing: The eastern Mediterranean case. *Earth and Planetary Science Letters*, *442*, 93–107.
Minelli, L., & Faccenna, C. (2010). Evolution of the Calabrian accretionary wedge (central Mediterranean). *Tectonics*, *29*, TC4004.
Moore, G. F., Boston, B. B., Strasser, M., Underwood, M. B., & Ratliff, R. A. (2015). Evolution of tectono-sedimentary systems in the Kumano basin, Nankai trough forearc. *Marine and Petroleum Geology*, *67*, 604–616.
Munch, J. (2020). *Physical controls on dynamics of spontaneously retreating subduction zones* (PhD Thesis). ETH Zurich.
Munch, J., Ueda, K., Gerya, T., & May, D. (2019). *Slab dynamics in the Caribbean, interactions between the deep and the shallow*. AGU Fall Meeting Abstracts.
Nicolosi, I., Speranza, F., & Chiappini, M. (2006). Ultrafast oceanic spreading of the Marsili basin, southern Tyrrhenian Sea: Evidence from magnetic anomaly analysis. *Geology*, *34*(9), 717–720. https://doi.org/10.1130/G22555.1
Noda, A. (2016). Forearc basins: Types, geometries, and relationships to subduction zone dynamics. *GSA Bulletin*, *128*, 879–895.
Pepe, F., Sulli, A., Bertotti, G., & Cella, F. (2010). Architecture and Neogene to Recent evolution of the Western Calabrian continental margin: An upper plate perspective to the Ionian subduction system, central Mediterranean. *Tectonics*, *29*, TC3007. https://doi.org/10.1029/2009TC002599
Pusok, A., & Kaus, B. (2015). Development of topography in 3-D continental-collision models. *Geochemistry, Geophysics, Geosystems*, *16*, 1378–1400.
Rosenbaum, G., & Lister, G. S. (2004). Neogene and Quaternary rollback evolution of the Tyrrhenian sea, the Apennines, and the Sicilian Maghrebides. *Tectonics*, *23*, TC1013.
Royden, L., Horváth, F., & Burchfiel, B. C. (1982). Transform faulting, extension, and subduction in the Carpathian Pannonian region. *GSA Bulletin*, *93*, 717–725.
Schellart, W. P., Freeman, J., Stegman, D. R., Moresi, L., & May, D. (2007). Evolution and diversity of subduction zones controlled by slab width. *Nature*, *446*, 308–311.
Schmid, S., Bernoulli, D., Fügenschuh, B., Matenco, L., Schefer, S., Schuster, R., et al. (2008). The Alpine-Carpathian-Dinaridic orogenic system: Correlation and evolution of tectonic units. *Swiss Journal of Geosciences*, *101*, 139–183.
Schmidt, M. W., & Poli, S. (1998). Experimentally based water budgets for dehydrating slabs and consequences for arc magma generation. *Earth and Planetary Science Letters*, *163*, 361–379.

Sengul-Uluocak, E., Pysklywec, R. N., Gogus, O. H., & Ulugergerli, E. U. (2019). Multidimensional geodynamic modeling in the Sout heastCarpathians: Upper mantle flow-induced SurfaceTopography anomalies. *Geochemistry, Geophysics, Geosystems*, *20*, 3134–3449.

Shemenda, A. I. (1993). Subduction of the lithosphere and back arc dynamics: Insights from physical modeling. *Journal of Geophysical Research*, *98*, 167–185.

Sinclair, H. (1997). Flysch to molasses transition in peripheral foreland basin: The role of the passive margin versus slab break-of. *Geology*, *25*(12), 1123–1126.

Sizova, E., Gerya, T., Brown, M., & Perchuk, L. L. (2010). Subduction styles in the Precambrian: Insight from numerical experiments. *Lithos*, *116*, 209–229.

Sobolev, S. V., & Brown, M. (2019). Surface erosion events controlled the evolution of plate tectonics on Earth. *Nature*, *570*(7759), 52. https://doi.org/10.1038/s41586-019-1258-4

Sokoutis, D., Corti, G., Bonini, M., Brun, J. P., Cloetingh, S., Mauduit, T., & Manetti, P. (2007). Modeling the extension of heterogeneous hot lithosphere. *Tectono-physics*, 63–79. https://doi.org/10.1016/j.tecto.2007.08.012

Spakman, W., & Wortel, R. (2004). A tomographic view on Western Mediterranean geodynamics. In W. Cavazza, F. Roure, W. Spakman, G. M. Stampfli, & P. A. Ziegler (Eds.), *The TRANSMED Atlas. The Mediterranean region from crust to mantle*. Springer. https://doi.org/10.1007/978-3-642-18919-7_2

Tackley, P. J. (2000). Mantle convection and plate tectonics: Toward an integrated physical and chemical theory. *Science*, *288*, 2002–2007.

Tari, G., Dovenyi, P., Dunkl, I., Horvath, F., Lenkey, L., Stefanescu, M., et al. (1999). Lithospheric structure of the Pannonian basin derived from seismic, gravity and geothermal data. In B. Durand, L. Jolivet, F. Horvath, & M. Serrane (Eds.), *The Mediterranean Basins: Extension Within the Alpine Orogen* (Vol. 156, pp. 215–250). Geological Society, London, Special Publications.

Tesauro, M., Kaban, M. K., & Cloetingh, S., (2009). A new thermal and rheological model of the European lithosphere. *Tectonophysics*, *476*, 478–495. https://doi.org/10.1016/j.tecto.2009.07.022

Tilita, M., Matenco, L., Dinu, C., Ionescu, L., & Cloetingh, S. (2013). Understanding the kinematic evolution and Genesis of a back-arc continental "sag" basin: The Neogene evolution of the Transylvanian Basin. *Tectonophysics*, *602*, 237–258. https://doi.org/10.1016/j.tecto.2012.12.029

Torne, M., Fernandez, M., Comas, M. C., & Soto, J. I. (2000). Lithospheric structure beneath the Alboran Basin: Results from 3D gravity modeling and tectonic relevance. *Journal of Geophysical Research*, *105*, 3209–3228.

Toth, J., & Gurnis, M. (1998). Dynamics of subduction initiation at preexisting fault zones. *Journal of Geophysical Research*, *103*(B8), 18053–18067.

Turcotte, D. L., & Schubert, G. (2002). *Geodynamics*. Cambridge University Press. https://doi.org/10.1017/CBO9780511807442

Ustaszewski, K., Kounov, A., Schmid, S. M., Schaltegger, U., Krenn, E., Frank, W., & Fügenschuh, B. (2010). Evolution of the Adria-Europe plate boundary in the northern Dinarides: From continent-continent collision to back-arc extension. *Tectonics*, *29*, TC6017. https://doi.org/10.1029/2010tc002668

van Dinther, Y., Preiswerk, L. E., & Gerya, T. V. (2019). A Secondary zone of uplift due to Megathrust earthquakes. *Pure and Applied Geophysics*, *176*, 4043–4068.

van Hinsbergen, D. J., Torsvik, T. H., Schmid, S. M., Matenco, L. C., Maffione, M., Vissers, R. L., et al. (2020). Orogenic architecture of the Mediterranean region and kinematic reconstruction of its tectonic evolution since the Triassic. *Gondwana Research*, *81*, 79–229.

van Hunen, J., van den Berg, A., & Vlaar, N. J. (2000). A thermo-mechanical model of horizontal subduction below an overriding plate. *Earth and Planetary Science Letters*, *182*, 157–169.

van Hunen, J., van den Berg, A. P., & Vlaar, N. J. (2004). Various mechanisms to induce present-day shallow flat subduction and implications for the younger Earth: A numerical parameter study. *Physics of the Earth and Planetary Interiors*, *146*, 179–194.

Vergés, J., & Fernàndez, M. (2012). Tethys–atlantic interaction along the Iberia–Africa plate boundary: The Betic–Rif orogenic system. *Tectonophysics*, *579*, 144–172.

Villasenor, A., Chevrot, S., Harnafi, M., Gallart, J., Pazos, A., Serrano, I., et al. (2015). Subduction and volcanism in the Iberia-North Africa collision zone from tomographic images of the upper mantle. *Tectonophysics*, *663*, 238–249.

Vogt, K., Gerya, T. V., & Castro, A. (2012). Crustal growth at active continental margins: Numerical modeling. *Physics of the Earth and Planetary Interiors*, *192*, 1–20.

Wallace, L. M., Ellis, S., & Mann, P. (2009). Collisional model for rapid fore-arc block rotations, arc curvature, and episodic back-arc rifting in subduction settings. *Geochemistry, Geophysics, Geosystems*, *10*, Q05001. https://doi.org/10.1029/2008GC002220

Whipple, K. (2009). The influence of climate on the tectonic evolution of mountain belts. *Nature Geoscience*, *2*, 97–104.

Wolf, S. G., & Huismans, R. S. (2019). Mountain building or backarc extension in ocean-continent subduction systems: A function of back-arc lithospheric strength and absolute plate velocities. *Journal of Geophysical Research: Solid Earth*, *124*, 7461–7482. https://doi.org/10.1029/2018JB017171

Wortel, M. J. R., & Spakman, W. (2000). Subduction and slab detachment in the Mediterranean–Carpathian region. *Science*, *209*, 1910–1917.

Yang, S., Li, Z.-H., Wan, B., Chen, L., & Kaus, B. (2021). Subduction-induced back-arc extension versus far-field stretching: Contrasting Modes for continental marginal break-up. *Geochemistry, Geophysics, Geosystems*, *22*, e2020GC009416. https://doi.org/10.1029/2020GC009416

Zhong, S., & Gurnis, M. (1992). Viscous flow model of a subduction zone with a faulted lithosphere: Long and short wavelength topography, gravity and geoid. *Geophysical Research Letters*, *19*, 1891–1894.

Zhong, S., & Gurnis, M. (1994). Role of plates and temperature-dependent viscosity in phase change dynamics. *Journal of Geophysical Research*, *99*, 15903–15917.

Zito, G., Mongelli, F., de Lorenzo, S., & Doglioni, C. (2003). Heat flow and geodynamics in the Tyrrhenian sea. *Terra Nova*, *15*, 425–432.